Aberystwyth University

A Full-Stokes 3D Calving Model applied to a large Greenlandic Glacier
Todd, Joe; Christoffersen, Poul; Zwinger, Thomas; Råback, Peter; Chauché, Nolwenn; Benn, Douglas ; Luckman, Adrian J.; Ryan, Johnny ; Toberg, Nick; Slater, Donald; Hubbard, Alun

A Full-Stokes 3D Calving Model applied to a large Greenlandic Glacier

Joe Todd[1], Poul Christoffersen[2], Thomas Zwinger[3], Peter Råback[3], Nolwenn Chauché[4], Doug Benn[1], Adrian Luckman[5], Johnny Ryan[6], Nick Toberg[2], Donald Slater[7], Alun Hubbard[6,8]

[1]Department of Geography and Sustainable Development, University of St Andrews, UK, [2]Scott Polar Research Institute, University of Cambridge, UK, [3]CSC - IT Centre for Science, Espoo, Finland, [4]Access Arctic SARL, [5]Department of Geography, College of Science, Swansea University, UK, [6]Centre for Glaciology, Institute of Geography and Earth Sciences, Aberystwyth University, Aberystwyth, SY23 3DB, UK, [7]School of Geosciences, University of Edinburgh, UK, [8]Centre for Arctic Gas Hydrate, Environment and Climate, Department of Geology, The Arctic University of Norway, 9 N-9037 Tromsø, Norway.

Corresponding author: Joe Todd (jat39@st-andrews.ac.uk)

Key Points:

- A 3D full-Stokes calving model was implemented in Elmer/Ice and applied to Store Glacier in West Greenland.

- The model reproduces the seasonal characteristics of ice flow and calving without tuning.

- Ice mélange and submarine melting link calving to the ocean, strongly modulated by basal topography.

Abstract

Iceberg calving accounts for around half of all mass loss from both the Greenland and Antarctic ice sheets. The diverse nature of calving and its complex links to both internal dynamics and climate make it challenging to incorporate into models of glaciers and ice sheets. Here, we present results from a new open-source 3D full-Stokes calving model developed in Elmer/Ice. The calving model implements the crevasse depth criterion, which states that calving occurs when surface and basal crevasses penetrate the full thickness of the glacier. The model also implements a new 3D rediscretization approach and a time-evolution scheme which allow the calving front to evolve realistically through time. We test the model in an application to Store Glacier, one of the largest outlet glaciers in West Greenland, and find that it realistically simulates the seasonal advance and retreat when two principal environmental forcings are applied. These forcings are 1) submarine melting in distributed and concentrated forms, and 2) ice mélange buttressing. We find that ice mélange buttressing is primarily responsible for Store Glacier's seasonal advance and retreat. Distributed submarine melting prevents the glacier from forming a permanent floating tongue, while concentrated plume melting has a disproportionately large and potentially destabilizing effect on the calving front position. Our results also highlight the importance of basal topography, which exerts a strong control on calving, explaining why Store Glacier has remained stable during a period when neighboring glaciers have undergone prolonged interannual retreat.

1 Introduction

Iceberg calving is the single most important ablation mechanism for Earth's polar ice sheets. In Antarctica, ice is lost primarily by calving and secondarily by bottom melting on ice shelves (Depoorter et al., 2013). In Greenland, ice is lost by calving and surface melting, with the former accounting for two-thirds of the total ice loss in the 2000s (Rignot and Kanagaratnam, 2006), but less than half since 2010 (Enderlin et al., 2014). The variability of ice lost by calving in Greenland is thought to stem from a sensitive interaction of the ice sheet with the ocean (Holland et al, 2008), which brought warm waters into coastal seas in the 2000s (Christoffersen et al., 2011). Understanding how the ocean forces the ice sheet through calving is therefore vital.

Calving processes and their links to glacier and ice sheet dynamics are poorly understood for various reasons. First and foremost, calving includes fracture processes spanning a range of temporal and spatial scales, from the relatively slow propagation of several kilometer long rifts in Antarctica (Bassis et al., 2008) to the initiation and growth of micro-fractures in glacier ice (Borstadt et al., 2012). Calving glaciers are diverse in their geometry and environmental setting, and their flow is largely controlled by conditions and processes operating at the ice-ocean interface and at the bed, all of which are difficult to observe. This complexity, combined with a paucity of data, makes dynamic mass loss from calving glaciers one of the most poorly constrained contributors to sea level rise in the 21st century and beyond (IPCC, 2013).

Early calving models focused on empirical relationships between calving and parameters such as water depth (Brown et al., 1982) or height above buoyancy (van der Veen, 1996, Vieli et al., 2001). Recent efforts have focused on using the near-terminus stress field to predict calving (van der Veen, 1998a, van der Veen, 1998b, Benn et al., 2007a,b, Alley et al., 2008, Levermann et al., 2012, Morlighem et al., 2016). Benn et al. (2007a) introduced the

crevasse depth calving criterion, suggesting that calving occurs when surface crevasses reach sea (or lake) level, at which point hydrofracture drives crevasses through the full glacier thickness. A modification by Nick et al. (2010) suggested that calving occurs when surface and basal crevasses collectively fracture the entire ice thickness near the terminus. These crevasse depth calving criteria have been implemented by several previous modelling studies (Nick et al., 2010, Otero et al., 2010, Vieli and Nick, 2011, Cook et al., 2012, Cook et al., 2014, Todd & Christoffersen, 2014; Pollard et al., 2015). To date, however, these models have either been implemented in only one or two dimensions, representing either flowline or depth-integrated glacier geometries, or do not permit evolution of the model domain through time. These limitations mean that the models inadequately capture important aspects of the calving mechanism, such as forward toppling due to terminus force imbalance, bending forces due to buoyancy, or the effect of lateral stress bridges. Simplified model domains also struggle to capture the impact of environmental forcings, which commonly include significant and spatially variable undercutting of the ice front by submarine melting (Luckman et al., 2015).

Here we develop a 3D time-evolving full-Stokes calving model incorporating a modified crevasse depth calving model, in the glaciological model Elmer/Ice (Zwinger et al. 2007, Zwinger and Moore, 2009, Gagliardini et al. 2013). In addition to the implementation of the crevasse depth calving criterion, a re-discretization scheme is developed which allows complex terminus geometries to evolve through time without requiring the simulation to stop and restart. We present results from a case study of Store Glacier, a large tidewater glacier in West Greenland (Fig. 1) to illustrate the capabilities of the model and provide some preliminary model validation. A full sensitivity analysis is available in the PhD thesis associated with this work (Todd, 2017).

2 Methods

2.1 Modelling Calving in 3D

We implement the 3D calving model in the open-source glaciological model Elmer/Ice. Elmer/Ice is able to solve the full-Stokes stress solution with excellent scalability, tracks grounding line dynamics and provides inverse methods for basal (and internal) conditions. In this section we describe the calving model and its implementation in Elmer/Ice, before describing the model setup, including boundary conditions, in more detail. Detailed descriptions of parts of the calving and remeshing algorithms are provided as supporting text, and the model code is freely available as part of the open-source Elmer/Ice package (http://elmerice.elmerfem.org).

2.1.1 Physical Calving Criteria

We implement an improved formulation of the crevasse depth calving criterion (Benn et al., 2007a; Nick et al., 2010), which predicts calving based on the penetration of crevasses. Two variants of the crevasse depth calving criterion exist: the original formulation of Benn et al. (2007a) specifies calving to occur when surface crevasses meet the waterline, at which point water flows in from the proglacial water body causing hydrofracturing which leads to full thickness calving. This process may occur even at cold glaciers because the exchange of heat between intruding proglacial water and glacier crevasses/conduits should prevent them from

freezing. An alternative crevasse criterion developed by Nick et al. (2010) considers the formation of basal crevasses, and states that calving occurs when surface and basal crevasses meet. We consider both of these criteria to be feasible and implement both, which means that calving in our model occurs when either condition is met.

To predict the penetration of surface and basal crevasses, we follow previous studies (Benn et al. 2007a, Nick et al., 2010, Otero et al. 2010) in using the Nye (1957) criterion, which we modify for use in 3D, as described below. The Nye criterion is a simplified approach to predicting the extent of a *field of closely spaced crevasses*, as opposed to tracking the evolution of individual crevasses. Extension in the direction of flow dominates the stress field near calving termini, and this longitudinal extension opens fields of crevasses largely through Mode 1 fracture (van der Veen, 1998b, Benn et al. 2007b). The Nye criterion predicts the opening of crevasses based solely on the extensional stress across the crevasse, making it the natural choice as a calving predictor.

Unlike the more complex Linear Elastic Fracture Mechanics (LEFM) approach (van der Veen, 1998a, 1998b, Krug et al., 2014), the Nye criterion ignores stress concentration effects, which are negligible under the assumption of closely spaced crevasses (Cuffey and Patterson, 2010), and so does not require prior knowledge of crevasse spacing. Additionally, the Nye criterion has no free parameters, meaning the calving law cannot be calibrated to observations. This allows us to more reliably assess the performance of the model. We also note that the focus of this study is the development of the modelling framework which allows time evolving calving in 3D continuum simulations; other calving laws could easily be implemented.

Nye (1957) noted that, in the case of negligible surface slope, tensile stresses exist to a depth (d) where:

$$\rho g d = 2\tau_{xx}$$ Eq. 1

where ρ is ice density, g is gravity and τ_{xx} is longitudinal deviatoric stress. This equation effectively splits the Cauchy, or full, stress (σ) into the ice overburden pressure on the left, and the deviatoric stress term ($2\tau_{xx}$) on the right. This assumes firstly that the hydrostatic pressure assumption is valid ($p = -\rho g d$) and secondly that τ_{xx} is constant through depth. These assumptions allow crevasse penetration to be estimated purely from surface measurements (Mottram and Benn, 2009). This 'observational' formulation of the crevasse depth is further exemplified by the work of Benn et al. (2007a) who use Glen's flow law to substitute the deviatoric stress term with a strain rate term.

Since we solve the full-Stokes flow solution, it is neither necessary nor desirable to split the Cauchy stress (σ) into its hydrostatic and deviatoric components; instead, the Cauchy stress can be computed everywhere directly from the flow solution. In this case, the Nye (1957) crevasse depth model states that crevasses should exist to a depth where:

$$\sigma_{xx} = 0$$ Eq. 2

which illustrates the simplicity of the Nye (1957) criterion, which states that crevasses exist where extensional stress exists to open them. This zero stress formulation ignores the yield strength which must be overcome to initiate fracture (Cuffey & Patterson, 2010) and we

justify this on the basis that ice near the front of calving glaciers is already heavily fractured (i.e. extensional stresses propagate existing fractures).

We make one further modification to Eq. 2, replacing σ_{xx}, which is unsuitable for modelling calving in 3D (Otero et al. 2010), with the largest principal stress:

$$\sigma_1 = 0 \qquad \qquad \text{Eq. 2b}$$

This modification is based on the assumption that crevasses on glaciers open by Mode I fracture (van der Veen, 1998b, Benn et al. 2007b), so that crevasses are expected to open perpendicular to the largest extensional stress (σ_1). This approach neglects crevasse history, but we find that surface crevasses in satellite imagery of Store Glacier tend to follow modelled principal stress direction which, in turn, tends to follow flow direction, especially near the terminus.

Equation 2b defines the depth of a surface crevasse field. To implement this in the model, we define, for both surface and basal crevasses, an Effective Principal Stress (*EPS*) whose value is positive where crevasses exist, and negative where ice is intact:

$$EPS_{surf} = \sigma_1 \qquad \qquad \text{Eq. 3}$$
$$EPS_{basal} = \sigma_1 + P_w \qquad \qquad \text{Eq. 4}$$

Water pressure (P_w) is included in Eq. 4 because calving glaciers typically experience high basal water pressure, which is essential for the opening of basal crevasses. Surface crevasses, on the other hand, are capable of opening without water pressure. Although previous work has specified water pressure in surface crevasses, we deliberately avoid this assumption because aerial photography has shown only a small number of Store Glacier's surface crevasses to be water-filled during summer (Ryan et al., 2015). Furthermore, the presence and depth of this surface meltwater in crevasses is extremely difficult to predict, depending not only on surface melt rates, but also crevasse spacing and geometry and the supra- and englacial drainage systems, which are poorly constrained. We therefore choose to ignore this process.

Basal water pressure, on the other hand, is controlled by the subglacial hydrological system, which is important for glaciers in general but especially important for glaciers terminating in deep fjords. Because modelling of the subglacial system is non-trivial and beyond the scope of this work, we make the reasonable assumption that basal water pressure, near the calving terminus, is equal to the pressure exerted by the sea at the terminus. The water pressure at the base of the glacier (P_{wb}) near the terminus is therefore:

$$P_{wb} = (z_{sl} - z_b)\rho_{sw}g \qquad \qquad \text{Eq. 5}$$

where Z_{sl} and Z_b are the elevation of sea level and the base of the glacier respectively and ρ_{sw} is the density of seawater. Given that basal crevasses will fill with buoyant freshwater from the subglacial hydrological system, the water pressure inside a basal crevasse (P_w) is then given by:

$$P_w = P_{wb} - (z - z_b)\rho_{fw}g \qquad \qquad \text{Eq. 6}$$

where ρ_{fw} is the density of freshwater and z is elevation.

2.2 Calving Algorithm in 3D

In 3D, calving requires full crevasse penetration along an uninterrupted line connecting two points at the terminus, thereby isolating a portion of the front from the remainder of the glacier. This makes the algorithm for identifying calving events in 3D significantly more complex compared to flowline models (Nick et al. 2010, Cook et al. 2012, Todd and Christoffersen, 2014) in which calving position is defined by a point along the length of the glacier. The change in glacier geometry after a calving event is also more complex in 3D. In flowline models, the geometry of a calving event is sufficiently simple that the initial model mesh can simply be stretched or compressed in the direction of flow to accommodate the new shape (Todd & Christoffersen, 2014). However, in 3D, the development of headlands and embayments, as well as undercutting, mean that the model mesh quickly becomes degenerate, whereby 3D elements change topology, leading to simulation breakdown. Thus, re-discretization of the domain ("remeshing") is required after calving events, to prevent the mesh from becoming degenerate.

2.2.1 Calving algorithm and its implementation

The calving model runs at the end of each timestep, after the computation of the flow solution and stress field. The full algorithm for identifying calving is shown in Fig. 2. The overall strategy is to first compute the 3D extent of crevasse fields on the model mesh, then collapse this via vertical ray casting and interpolation into a 2D map of crevasse depth on a separate planar mesh (Fig. 3). Finally, calving events are identified on the planar mesh.

First, EPS_{surf} and EPS_{basal} (Eqs. 3, 4) are computed everywhere in the 3D domain, to determine where surface and basal crevasses exist. This is then collapsed to a 2D field of crevasse penetration (H_{crev}) on the planar mesh "PlaneMesh" (Fig. 3). PlaneMesh is independent of the main model mesh; it encompasses the whole terminus region, extending 3km upstream from the calving front. It also has a higher resolution (30 m) than the main model mesh. For each node in PlaneMesh, vertical ray casting is used to find a vertical profile through the main model mesh, from which proportional crevasse penetration (H_{crev}) is computed on the basis of ice thickness and the depths of surface and basal crevasses:

$$H_{crev(surf)} = \frac{d_{surf}}{z} \qquad \text{Eq. 7}$$

$$H_{crev(basal)} = \frac{d_{surf} + d_{basal}}{H} \qquad \text{Eq. 8}$$

where d_{surf} and d_{basal} represent the depth of surface and basal crevasses respectively, z is the ice freeboard, and H is the ice thickness. H_{crev} is equal to 1 where crevasses penetrate fully, and between 0 and 0.99 elsewhere (Fig. 4). We then use the $H_{crev} = 1$ contours to identify potential calving events specified by a line of full crevasse penetration intersecting the ice/ocean interface at two locations. However, this was found to be an insufficient condition for calving; sometimes $H_{crev} = 1$ contours form constrictions, before widening inland. In such cases, crevassed ice is laterally constrained by intact ice, and so cannot be evacuated into the fjord. Therefore, we add an extra filter in the calving algorithm (Text S1), which automatically checks that the ice that calves off has a realistic geometry. This control inspects the geometry of the $H_{crev} = 1$ contour and specifically ensures that ice cannot be lost through

narrow constrictions. When a narrow constriction is found, the $H_{crev} = 1$ contour is cut to make sure unphysical calving is prevented.

The final stage of the calving algorithm is to identify points on the 3D calving front that lie within a region predicted to calve; for each 3D mesh node on the calving front, we seek an upstream $H_{crev} = 1$ contour line and, if found, mark the post-calving position of the node, which lies on this contour. For any node for which a corresponding post-calved position is found, we compute the 'calving vector', perpendicular to the overall orientation of the calving front, which represents the displacement from the pre-calved position to the post-calved position (Fig. S6a). The calving vector is then passed to the remeshing algorithm, which displaces the calving front before beginning the remeshing.

We note that the model mesh is initially produced through vertical extrusion. If there were no undercutting or depth-dependent ice flow, the calving front would remain vertical and internal nodes would be arranged in vertical columns, making ray casting and interpolation onto a separate mesh unnecessary. This is, however, an idealized situation and we consider the non-vertical and evolving ice front to be a salient feature of our model.

2.2.3 Projectability of the Calving Front

The current remeshing implementation requires that the calving ice front remains projectable in some arbitrary coordinate system (chosen based on the orientation of the terminus). Essentially, this means the ice-ocean interface is not permitted to 'overlap' itself in the direction of flow (Fig. S6b). The effect that this projectability requirement has on the calving algorithm is that any ice which is directly downstream of a calving event is also calved. On the whole, this requirement of projectability should not be a major limitation, as a consideration of stress and calving stability would suggest that significant overlap of this kind would be difficult for a real glacier terminus to sustain.

2.2.4 Time-stepping

Calving events involve a change in terminus geometry which affects the state of stress in the glacier. As such, it is often possible for a calving event to immediately trigger subsequent calving events (Chapuis and Tetzlaff, 2014; O'Neel et al. 2004). For example, the two calving events shown in Figure 4a leave an exposed headland between them (Fig. 4b) which would then calve due to the loss of lateral support. However, in a typical time-evolving model, these secondary calving events cannot occur until the next timestep, introducing an artificial delay in the calving rate. The instantaneous nature of this effect means that it cannot be solved by simply reducing the timestep size.

In order to overcome this limitation, a time-stepping scheme was developed whereby, following a large calving event ($> 1.0 \times 10^6$ m^3), we effectively "pause" the simulation to recompute the velocity, stress and calving criterion. We iterate until no more calving events occur and then resume the time evolution. We specify a minimum iceberg size for pausing because testing revealed that very small calving events were sometimes followed by other small events from different parts of the terminus. These are not genuine secondary calving events, but rather a result of the re-discretization of the model mesh slightly altering the stress field. The size threshold ensures that the model is only paused following calving events which can significantly alter the stress field.

2.3 Remeshing Algorithm

Remeshing is performed after every calving event. This involves the production of a new mesh from the post-calving geometry (rediscretization), and the interpolation of the field variables from the old to the new mesh. The remeshing algorithm is described in detail in Text S2 and illustrated in Figures S3 and S4.

3 Application of 3D calving model to Store Glacier, West Greenland

To illustrate model performance, we implement the calving and remeshing scheme described above into a time-evolving simulation of the dynamics of Store Glacier, West Greenland. The model is implemented in the finite element model Elmer/Ice, and makes extensive use of the existing glaciological code therein. The model implementation is described below, and summarised in Figure S5.

3.1 Setting and flow of Store Glacier

Store Glacier (Fig. 1) is the second largest outlet glacier in West Greenland in terms of ice flux (Weidick and Bennike, 2007). Store Glacier's ice catchment extends 280 km inland to the ice divide, and has a maximum width of 50 km which narrows to 5 km at the terminus, where velocity typically peaks at around 16 m d^{-1} (~5800 m a^{-1}). Initial surface elevation is taken from the GIMP DEM product (Howat et al., 2015). We use a mass-conservation approach, constrained by thickness data from Operation IceBridge flight lines (https://espo.nasa.gov/missions/oib/), to determine Store Glacier's basal topography near the terminus (Todd & Christoffersen, 2014). At the terminus, this mass-conservation DEM is merged with bathymetric data collected adjacent to Store Glacier's terminus by S/V Gambo in July, 2012.

Store Glacier's calving ice front advances several hundred metres in winter and retreats equivalently in summer, and has remained stable in its mean annual position during a period of at least 40 years which saw many glaciers in the Uummannaq region and elsewhere undergoing substantial retreat (Howat et al. 2010). Basal topography reveals that upstream of a large basal pinning point at the terminus, the glacier flows through a 30 km long overdeepening, reaching a depth of 900 m below sea level. As well as the basal pinning point, Store Glacier's terminus calves at a lateral valley constriction, which also contributes to its stability.

Aerial photography from Store Glacier (Ryan et al., 2015) indicates the presence of concentrated meltwater plumes at locations where vigorous upwelling is driven by localised subglacial discharge into the fjord. Direct observation of submarine melt rates at Store Glacier (Chauché, 2016) shows that there is a large degree of horizontal variability due to these concentrated plumes. In addition, both modelling (Rignot et al., 2016) and observations (Chauché, 2016) for Store Glacier indicate significant seasonal variability, with large volumes of surface meltwater being subglacial discharged in summer while winter discharge is limited to meltwater produced along the bed by frictional and geothermal heat fluxes.

Another important environmental process is the seasonal formation of ice mélange which buttresses the front of Store Glacier during the winter and spring (Howat et al. 2010). Under the assumption that all other environmental forcing remains constant, the buttressing exerted by seasonal mélange can be estimated from the velocity perturbation observed at the terminus

as a result of its breakup. Walter et al. (2012) estimate a ~1.5 m d^{-1} terminus velocity perturbation during breakup in late May 2008 from time-lapse camera imagery, from which they infer a mélange buttressing force of 30-60 kPa at Store Glacier. Here, we justify a higher value for the buttressing force of 120 kPa based on a mean terminus velocity perturbation of ~4 m d^{-1} determined from repeat UAV surveys conducted from 4 - 8 June, 2014, during the period of mélange breakout (Hubbard et al., 2015; Toberg et al., 2016).

3.2 3D Model Domain

We choose a model domain that extends 112 km inland from Store Glacier's calving terminus and laterally follows the edges of the glacier's ice catchment (Fig. 5). The length and width of the domain ensures that the terminus is far removed from any boundary effects. The initial model mesh is produced by extruding a 2D footprint mesh, produced in GMSH, to 15 internal layers of equal thickness using Elmer/Ice's internal mesh extrusion scheme (Gagliardini et al., 2013). Horizontal mesh resolution varies from 100m at the terminus to 2km in the interior (Fig. 1).

The domain is constrained by 6 boundary conditions: the base of the ice (Γ_{base}), the upper ice surface (Γ_{surf}), the inflow (Γ_{inflow}), the calving front (Γ_{term}), and the two lateral boundaries (Γ_{left} and Γ_{right}). In the case of the basal boundary condition, we distinguish between grounded ice ($\Gamma_{\text{base-G}}$) and floating ice ($\Gamma_{\text{base-F}}$).

3.3 Ice Dynamics & Temperature

The model solves the full-Stokes equations for ice flow, with rheology defined by Glen's flow law (Cuffey and Patterson, 2010). During the spin-up phase, described below, we solve the coupled dynamics/temperature system. During the 5-year calving simulations, we keep the temperature field fixed and solve only for the velocity, as the short timescale of these simulations permits decoupling of temperature from velocity. This allows us to account for the effect of temperature on ice viscosity while maintaining computational efficiency.

Ice temperature is fixed on the surface and inflow boundary using the MODIS IST product (http://modis-snow-ice.gsfc.nasa.gov/?c=greenland), averaged from 2000-2014. We account for heating due to basal friction and internal strain, as well as geothermal heat flux at 75 mW m^{-2} (Greve, 2005). The temperature dependent rate factor (A) in Glen's flow law is computed using the Arrhenius relation (Text S3).

On the inflow boundary (Γ_{inflow}), we prescribe annual mean observed surface velocity from TerraSAR-X derived surface velocity data:

$$\boldsymbol{u} = \boldsymbol{u}_{obs} \quad \text{on } \Gamma_{\text{inflow}} \qquad\qquad \text{Eq. 9}$$

where $\boldsymbol{u}$ is the velocity vector. The lateral boundaries (Γ_{left}, Γ_{right}) are aligned with the edge of Store Glacier's ice catchment, and so we impose a no penetration condition on these boundaries. The flow of ice along these boundaries is controlled by a prescribed slip coefficient (β). Thus, the lateral boundary condition is:

$$\boldsymbol{u} \cdot \boldsymbol{n} = 0 \quad \text{on } \Gamma_{left}, \Gamma_{right}, \Gamma_{base-G} \qquad\qquad \text{Eq. 10}$$

$$t \cdot (\boldsymbol{\sigma} \cdot \boldsymbol{n}) = -(\boldsymbol{u} \cdot t)\beta \quad \text{on } \Gamma_{left}, \Gamma_{right}, \Gamma_{base-G} \qquad \text{Eq. 11}$$

where $\boldsymbol{n}$ is the outward pointing surface normal, and **t** is either of the surface tangent vectors. The lateral friction coefficient (β) was tuned to match modelled and observed velocities at the lateral margins: at ice/rock interfaces the value is 1.0×10^{-2} and at ice/ice interfaces the value is 1.0×10^{-3}. For grounded ice, the basal boundary condition (Γ_{base-G}) is also described by Eqs. 10 & 11, although rather than prescribing a constant value for β we employ inverse methods to estimate the spatially and temporally variable β field, as described below.

When flotation occurs, basal traction disappears (Eq. 13) and motion in the surface-normal direction occurs in response to external pressure from the sea (Eq. 12):

$$\boldsymbol{n} \cdot (\boldsymbol{\sigma} \cdot \boldsymbol{n}) = \min(-\rho_w g(z - z_{sl}), 0) \quad \text{on } \Gamma_{base-f}, \Gamma_{term} \qquad \text{Eq. 12}$$
$$t \cdot (\boldsymbol{\sigma} \cdot \boldsymbol{n}) = 0 \quad \text{on } \Gamma_{base-f}, \Gamma_{term} \qquad \text{Eq. 13}$$

The stress boundary condition on the calving front (Γ_{term}) is identical to that for floating portions of the base (Eqs. 12, 13). The upper ice surface (Γ_{surf}) is stress free:

$$\boldsymbol{\sigma} \cdot \boldsymbol{n} = \boldsymbol{0} \quad \text{on } \Gamma_{term} \qquad \text{Eq. 14}$$

3.4 Surface Evolution

Both the upper and lower ice surfaces are free surfaces, and so their evolution must be computed at each timestep. The upper ice surface evolves in response to ice dynamics and surface mass balance (SMB). We apply seasonally constant SMB from RACMO 2.3 data (Noël et al., 2015), averaged over the period 1958-2013.

The base of the ice is a contact/grounding line problem. Under most of the domain, the base of the ice rests on the bedrock. However, high water pressure near the terminus can lead to flotation. We compute the evolution of the grounding line using Elmer/Ice's in-built grounding line subroutine (Durand et al., 2009a, Durand et al., 2009b, Favier et al., 2012), which compares the integrated external water pressure with the residual of the Stokes solution to determine grounding line contact during the nonlinear iteration of the flow solver. When flotation occurs and the floating region is connected to the proglacial fjord, we apply basal melting on the floating tongue at 1/10th of the maximum distributed melt rate applied on the much steeper calving front, described below.

3.5 Ice Front Evolution

The calving front in our model is also a free surface whose evolution must be computed. Unlike the upper and lower surfaces, front evolution occurs as a result of two distinct processes: continuous advance due to ice flow and instantaneous calving retreat. These processes are treated separately: calving loss is dealt with by the remeshing algorithm. Initially, the kinematic free surface equation, described above, was used to compute advance of the front, but this was found to be unstable due to the complex geometry of the front. Instead, we adopt a fully Lagrangian approach, in which the nodes on the terminus are free to move in any direction in response to velocity and ablation. In this approach, the displacement of nodes is a vector (d) defined by:

$$\boldsymbol{d} = (\boldsymbol{u} + a_\perp \boldsymbol{n})dt \hspace{4cm} \text{Eq. 15}$$

where $a_\perp$ is accumulation normal to the front, dt is the timestep size and $\boldsymbol{n}$ is the outward pointing normal vector.

3.6 Model Spin Up

Inverse methods were used to determine basal slip underneath the model domain. Velocity maps from 20 TerraSAR-X image pairs spanning April 2014 - April 2015 were used to constrain the seasonal evolution of the basal slip parameter (β, Eq. 11) using the adjoint method (Gillet-Chaulet et al., 2012). The resulting β maps were used to drive seasonal velocity fluctuations in the forward model.

The inversion strategy was complicated by the evolution of the upper ice surface; changes in driving stress caused the velocity field to drift. Thus, it was necessary to first iterate between phases of surface evolution and basal inversion. In this phase of the spin-up, annual average velocity was used for the inversion. After sufficient surface relaxation, the 20 seasonal inversions were computed, and the seasonally evolving forward model was spun up for 300 years at a 0.05 year timestep. During this spin-up the terminus position remained fixed and the calving model was not active, as it requires up to 100 times as many timesteps per year of simulation time. This simplification is justified by Store Glacier's stable terminus position.

3.7 Model Forcing

The two principal processes investigated in this study are undercutting of the calving ice front by submarine melting and buttressing by proglacial ice mélange, both of which exhibit strong seasonal variability. In addition, we incorporate seasonal changes in basal traction, which drive seasonal variability in ice velocity.

3.7.1 Ice Mélange

We impose the buttressing force from seasonally rigid ice mélange as an external pressure on the terminus, starting on 1st Feb and ending on 29th May each year, consistent with observations (Howat et al., 2010). We apply buttressing at a value of 120 kPa, over a thickness of 140m, These estimates are based on surveys of the mélange in front of Store in 2014 (Toberg et al., 2016).

3.7.2 Submarine Melting

We implement submarine melting as an ablation term in the frontal surface evolution (Eq. 15), applied normal to the surface. Unlike flowline models (Cook et al. 2012, Todd & Christoffersen 2014), the 3D model allows laterally heterogeneous melting to be investigated. We split frontal melting into 'distributed plume' melt rate covering the entire submerged ice front, and 'concentrated plume' melting at higher rates, imposed at two locations where these concentrated plumes are persistently observed (Fig. 5c).

Point and line source buoyant plume models (Slater et al., 2016) were used to determine melt profiles from concentrated and distributed plumes respectively. These plume models allow

realistic plume geometries to be obtained from simple inputs, rather than fully resolving fjord dynamics, which is beyond the scope of this study.

The plume models are driven with subglacial discharge values which maintain consistency with observed plume melt rates. The distributed melt profile is constrained by front-averaged melt rates for summer (3.1 m d^{-1}) and winter (1.3 m d^{-1}) consistent with observations (Chauché et al., 2016) as well as model results (Rignot et al., 2016). The concentrated melt profile is constrained by directly observed maximum in-plume melt rates of 12 m d^{-1} (Chauché et al., 2016).

Figure 5 shows concentrated plume width and melt profiles from the plume model. Distributed melting is applied at the summer rate from June to the end of August, the period when large volumes of surface meltwater enter the subglacial hydrological system (Chauché, 2016), and at the winter rate otherwise. Concentrated plume melting is applied only in summer. We assume that concentrated plume melt rates decay away from the plume centerline as a Gaussian curve (Turner, 1973):

$$m = m|_{x=0} \, e^{-\left(\frac{x}{W}\right)^2} \qquad \text{Eq. 16}$$

where x is the horizontal distance from the center of the plume and W is the width the of the plume at the given elevation.

Figure 5 shows that the predicted plume melt rates reach a maximum value between 5 and 200 m above the base of the ice front, due to low plume temperature below this point. The effect of these melt profiles is to produce a front which is undercut, but with small, sharp 'toes' remaining at the base. Slater et al., 2017 have shown that even with such melt profiles, toes may not form due to the shape of subglacial channels near the grounding line. On the other hand, such toes are known to exist in nature (Motyka, 1997; Warren et al., 1995) and tend to calve suddenly due to the buoyant force acting on them. We do not model subglacial channels, and the vertically integrated calving model presented here cannot physically capture these toe calving events. Hence, we impose "toe calving" within the frontal melting algorithm, essentially assuming that the buoyant force on these toes causes them to calve as soon as they form. We keep track of this mass loss, which is separate from submarine melting for the purposes of data analysis.

In addition to submarine melting of the vertical calving front, we impose basal melting underneath the floating portion of the terminus. Basal melt is imposed at 10% of the maximum distributed frontal melt rate, following the analysis of Jenkins (2011), which shows that the gentle slope of the ice base effectively limits melting. Basal melting under grounded ice is not included in this model.

3.8 Experimental Design

From the end of the 300 year spin-up phase, we run four combinations of three principal forcings i.e. ice mélange buttressing, distributed melting and concentrated melting (Table 1). Run 000 is our base run with no forcing, Run 001 includes distributed submarine melting only, Run 011 includes concentrated as well as distributed submarine melting while Run 111

includes ice mélange and both types of submarine melting. Run 111 therefore represents our best attempt at modelling the 'present day' conditions at Store Glacier. Seasonal variations in basal slip are imposed in all simulations, as this seasonal forcing is present in the spin-up, and so removing it would result in immediate glacier-wide divergence from steady-state.

4 Results

4.1 Seasonal response to forcing

Figure 6 shows the evolution of the model's terminus position and velocity in response to the four forcing combinations. The different forcings produce markedly different patterns of terminus evolution. In Run 000, in which only seasonally variable basal slip is applied, mean terminus position varies stochastically over an 800 m range without a seasonal signal. The simulations which include distributed submarine melting (Run 001) and concentrated as well as distributed submarine melting (Run 011) both produce a seasonal cycle of advance and retreat, with mean terminus position varying by around 200m. In Run 011 we find that concentrated melting triggers a temporary but substantial retreat of 400 m after 4.5 years. Although the retreat is recovered during the following winter, the absence of a similar retreat in Run 001, which included distributed melting only, signifies a potentially sensitive response to concentrated melting. We discuss this result in greater detail below.

Ice mélange (Run 111) exerts the greatest influence on seasonal terminus dynamics, causing a 500 m advance of the terminus each spring, followed by rapid retreat when the mélange disappears. The calving of a large tabular berg when the buttressing force from mélange vanishes (Fig. 7) is a consistent feature of our model. The model results also suggest that ice mélange helps stabilise the terminus against the impact of concentrated submarine melting; Run 111 does not undergo the significant retreat which occurs in Run 011 at 4.5 years (Fig. 6).

Only ice mélange is able to substantially influence the terminus velocity, which follows the same seasonal pattern in all other runs as a result of varying basal drag. In simulations without mélange, ice velocity peaks in early summer at 5100 m a^{-1}, before a deceleration through late summer to an annual minimum of 4200 m a^{-1}. Following this late-summer minimum, the velocity steadily increases through the winter. When buttressing from ice mélange is applied in February in Run 111, the terminus rapidly decelerates from 4800 m a^{-1} to 4150 m a^{-1} after which it gradually speeds up. At the end of May, when the buttressing force is removed, there is an equivalent rapid acceleration of ice flow at the terminus.

4.2 Terminus Mass Budget

The seasonal advance and retreat of the model terminus can be investigated as a balance between flow of ice towards the terminus and various mass loss components. Figure 8 shows changes in this terminus mass budget for the 'present-day' forcing simulation (Run 111). Influx through the flux gate (Fig. 5) is balanced by mass loss from calving, submarine melting and (negligible) surface melting. Table 2 compares the average annual terminus mass budget for all four simulations.

Iceberg calving dominates terminus mass loss in the present-day simulation (Fig. 8). In fact, 74% of the 8.96 Gt delivered to the terminus each year is lost through calving, with another

20% lost to distributed melting (Table 2). Concentrated melting accounts for only 1% of the total frontal ablation rate, yet calving in our model is quite sensitive to this process, as suggested above. Ice mélange greatly influences calving rate, which is reduced from around 10 Gt a^{-1} to less than 1 Gt a^{-1} at the start of the mélange season. As the terminus consequently advances, the calving rate gradually increases, but it is not until the end of the mélange season that the terminus ceases to advance. The ~1 Gt of mass gained by the terminus through its advance during each mélange season is rapidly lost when the mélange disappears. A large proportion of this rapid frontal mass loss is in the form of a large tabular berg (e.g. Fig. 7). Outside the mélange and melt seasons, loss through calving and melting balances influx towards the terminus, resulting in a stable terminus position.

Submarine melting, prescribed with different summer and winter rates, produces a clear stepped profile in frontal mass loss from melting (Fig. 8). The slight increase in melting during the mélange season stems from the terminus developing a floating tongue, thus increasing the area exposed to sea water and thus melting. As a result, the mean annual loss from submarine melting for Run 111 is 0.09 Gt a^{-1} greater than in Run 011.

Annual mean data (Table 2) reveals that terminus mass loss is dominated by calving in all simulations, though submarine melt processes remove a non-negligible quantity of ice when present. Concentrated submarine melting never accounts for more than 1% of mass loss (0.11 Gt a^{-1}), but Figure 6a demonstrates that this process can temporarily destabilise the terminus, causing retreat. In Run 001, which is forced with the same quantity of distributed melt, but has no concentrated plume, the terminus remained stable throughout the simulation. Run 111 demonstrates how the buttressing from ice mélange reduces the mean annual influx towards the terminus. This change is seen in Fig. 8, as a reduction from 9 to 8 Gt a^{-1} near the start of each year, and in Fig. 6 as a terminus deceleration of 500 m a^{-1}.

4.3 Spatial and Temporal Iceberg Distribution

The 3D calving model allows us to investigate calving at the individual event scale. Figure 9 shows the location, volume and season of every calved iceberg produced in each of the 5-year long simulations. Figure S7 shows the frequency distribution of all icebergs from Run 111.

In the absence of either ice mélange or submarine melting (Run 000), the modelled terminus advances a persistent floating tongue in the south (Fig. 9a) which calves predominantly large icebergs with no seasonal trend. The addition of distributed submarine melting (Run 001, Fig. 9b) prevents the formation of this floating tongue, and terminus position remains fairly fixed through the year. In Run 011, which includes concentrated as well as distributed melting (Fig. 9c), the seasonal calving cycle becomes more apparent, especially in the south where summer (0.4 - 0.6 years) calving events occur further upstream. However, there remains a dense distribution of calving events which delineates the typical terminus geometry. This pattern suggests that concentrated melting is able to promote calving and retreat in the south, but also that the terminus is quick to readvance when concentrated melting ceases.

Ice mélange buttressing (Run 111, Fig 9d) generates a stronger seasonal cycle in calving behaviour than either submarine melt component. Calving during the mélange season is consistently further downstream compared to the rest of the year, apart from two very large icebergs. Interestingly, the melt-season retreat of the southern floating region observed in Run 011 (Fig 9c) is absent, despite the application of concentrated submarine melting.

Calving behaviour is clearly dependent on the applied environmental forcing, but there are some persistent features. In all four simulations, the lateral margins of the terminus near the valley walls remain fixed in position and calve very small icebergs. The largest calving events in every simulation occur in the southern half of the terminus, which is floating. In the present-day forcing simulation (Run 111, Fig 9d), the five largest calving events in the south are an order of magnitude larger than those in the north. These tabular icebergs (e.g. Fig. 7) equate to 3.54 Gt mass loss between them, 11% of the total calving loss for the simulation.

5 Discussion

5.1 Crevasse Penetration in 3D

We can use our 3D model of Store Glacier to gain a better understanding of the processes that govern the calving mechanism in general. Figure 10 illustrates how calving in our model can be triggered by two conditions. Either surface crevasses reach the water line or surface and basal crevasses collectively intersect the full ice thickness. The two conditions for calving manifest themselves in distinctly different patterns in our model. The surface crevasses are widespread and display a generally smooth transition from relatively deep near the terminus to relatively shallow farther inland. The deeper penetration of surface crevasses towards the terminus is a result of extensional ice flow and the ice cliff force imbalance which further increases the extensional stress near the surface (Hanson & Hooke, 2003). The southern side of the terminus is dominated by a region of very low crevasse penetration which occurs just downstream of the modelled grounding line. The grounding line acts as a hinge point where upward bending forces act to close surface crevasses.

Compared to surface crevasses, the opening of basal crevasses is much more localised (Fig. 10b). Basal crevasses only form in ice which is at or near flotation, due to the requirement for high basal water pressure (Bassis and Walker, 2012, Ma et al., 2017). As a result, the southern side of the terminus experiences much more extensive basal crevassing than the north, which is mostly grounded. Furthermore, basal topography creates sharp transitions from compressive to extensive stress regimes, resulting in sharp boundaries between intact ice and deep basal crevasse fields.

The crevasse depth patterns shown in Fig. 10 are a consistent feature in our simulations, largely irrespective of the applied environmental forcing. This suggests that the observed crevasse patterns, and the resulting calving behaviour, are a product of the glacier geometry and topography. This finding is supported by previous calving modelling (Bassis & Jacobs, 2013, Krug et al. 2014, Ultee & Bassis, 2016) and remote sensing (Carr et al., 2013; McFadden et al., 2011; Moon et al., 2015) studies which highlight the importance of topography and geometry in determining calving style and glacier stability.

5.2 Model vs. Observations

In this section, we use satellite observations of surface elevation and terminus position, data not previously ingested into the model setup, to assess the performance of the calving model. We do not compare modelled versus observed velocities because, having inverted for basal friction, this comparison would be spurious. Figure 11 shows a surface DEM for Store Glacier's terminus overlain with the modelled grounding line position which neatly encompasses a distinct surface depression in the DEM.

The inset elevation profile clearly shows that the surface depression in the DEM forms a grounding line hinge point, a feature which the model successfully reproduces, and which indicates that the southern side of Store Glacier is floating up to 2 km inland from the terminus. This shows that the model successfully captures the detailed features of Store Glacier's grounding line dynamics. The upward bending moment at the grounding line hinge point, and the apparent downward bending closer to the front, are responsible for the distinct pattern of crevasses, which close and open in response to these bending forces (Fig. 10a).

There is, however, a discrepancy in surface elevation around the modelled grounding line. This is likely due to inaccuracies in the bed topography, which is determined indirectly from mass conservation. There is a large bedrock bump here (which is responsible for the steep surface slope) and it may be that the mass conservation approach smoothes this feature. Modelled and observed surface elevation converge once again upstream of the grounding line.

To further validate the 3D model, we extract terminus geometries from 24 TerraSAR-X images collected from April 2014 to April 2015 and compare the observed terminus evolution with that of the model. Figure 12 compares modelled and observed maximum, minimum and mean terminus positions for Run 111, as well as comparing mean terminus position through time

There is a close fit for the minimum front position, and a reasonable fit for the mean position, but the maximum terminus extent in the model is up to 1 km farther downstream than observed. In terms of the seasonal pattern of terminus advance and retreat, there is a close match between the model and observations (Fig. 12). Fast terminus advance begins in February and continues until May, in both the model and observations. This advance is followed by subsequent rapid retreat to a minimum terminus position in August. This retreat is followed by a slow and punctuated advance, which lasts until the start of the next winter when formation of the mélange once again promotes terminus advance.

The correspondence in the timing of advance and retreat strongly suggests that ice mélange drives seasonal changes in calving rate at Store Glacier. This is further supported by data from 1999-2010, which show a similar pattern of late winter advance when mélange is present and early summer retreat following mélange collapse (Howat et al. 2010). We note, however, that the model advances farther into the fjord than observed. Possible reasons for this are discussed below.

Overall, there is reasonably close agreement between the model and observed calving behaviour, especially considering that the calving model is uncalibrated, untuned, and forced with only three simplified environmental processes: undercutting by distributed and concentrated submarine melting and the buttressing effect from seasonally rigid ice mélange. We cannot exclude the possibility that other environmental processes are important in reality. Nevertheless, the match between model and observations lends support for the use of the dual crevasse depth criteria used to predict calving in this study. A prior study implementing the crevasse depth criterion in a 2D flowline model for Store Glacier (Todd & Christoffersen, 2014) did require tuning to produce realistic behaviour, suggesting that flowline models may be fundamentally unable to capture important calving processes at Store Glacier. Evidence of lateral variability in crevasse patterns (Fig. 11) (Ryan et al., 2015) and terminus position and range (Fig. 12) support this hypothesis.

5.3 Environmental Processes Affecting Calving

Our results indicate that the 3D calving model of Store Glacier is sensitive to present-day values of both submarine melting and ice mélange buttressing. We have also shown that the model's calving response to these processes is quite similar to observed. Distributed submarine melt plays an important role in the model, preventing the formation of a large and permanent floating tongue in the south (Fig. 9a,b). This suggests that submarine melting may play an important role in determining Store Glacier's current terminus position.

The addition of concentrated melting from two conical plumes led to substantial additional summer retreat at 4.5 years (Fig. 6a), despite those plumes contributing less than 5% of total melting. This increased seasonality is largely restricted to the floating southern portion of the terminus, where highly localised melt from these plumes progressively carves notches into the terminus, effectively isolating a portion of the terminus from the surrounding ice. Indentation of the ice front by localised melting effectively breaks stress bridges that provide lateral support to the ice front, a process that we term 'the keystone effect'. Through this mechanism, highly localised melt can trigger calving across a broad width of the terminus, amplifying its impact on rates of mass loss.

Our results thus indicate that the distribution of submarine melting may be more important than the total melt volume in terms of calving and terminus stability. Therefore, subglacial topography and hydrology, which control the location of concentrated buoyant plumes, may be of critical importance for the stability of calving glaciers. With more meltwater forming on the Greenland Ice Sheet as a consequence of climate change, we expect subglacial discharge into fjords to increase in the future. We thus expect the effect of concentrated plumes to become increasingly important for glaciers such as Store Glacier.

Ice mélange is the main driver of seasonal terminus position variability in the model, a finding which agrees with previous modelling studies (Vieli and Nick, 2011, Todd and Christoffersen, 2014, Krug et al. 2015) which found a significant effect on calving from ice mélange. In Run 111, mélange buttressing resulted in a mean advance of 500 m from winter to late spring. Figure 12 illustrates that the effect of the mélange is greatest in the southern part of the terminus, where the terminus reaches flotation and large seasonal advance occurs. We hypothesise that this is due to the difference in dynamics and stress across the terminus; an aspect we will continue to explore in future work.

In addition to driving seasonal cycles of advance and retreat, there are features of our model which indicate that ice mélange may stabilise the terminus against longer term retreat. Towards the end of Run 011, in which submarine melting is active but mélange is absent (Fig. 6), the terminus undergoes substantial retreat; this retreat does not occur in Run 111, suggesting that the mélange is exerting a stabilising influence on the terminus which extends beyond the mélange season. Mélange buttressing leads to deceleration and dynamic thickening of the terminus; this thickening stabilises the terminus against increased melting in summer.

Comparing model results to observations (Fig. 12) showed that the terminus in our model advances more than in reality when ice mélange is present. There are several potential reasons for this exaggerated effect. The application of a constant buttressing force is likely to be an oversimplification as glacier flow and especially large calving events probably disrupt and weaken the mélange, at least temporarily. Alternatively, the mélange buttressing pressure

used in this study, which were derived at the end of the mélange season, may not be representative of the buttressing effect over the whole season.

5.4 Resolving Calving in Ice Sheet Models

Modern ice sheet models (Blatter, 1995, Pattyn, 2003, Gudmundsson et al., 2012, Cornford et al. 2013) typically neglect vertical stress terms which are of secondary importance at the ice sheet scale; this makes the computation of ice dynamics for an entire ice-sheet computationally feasible. Furthermore, most prior calving modelling studies have implemented 1D and 2D flowline models for the sake of simplicity and efficiency (Nick et al. 2010, Vieli and Nick, 2011, Todd & Christoffersen, 2014, Cook et al. 2014). By contrast, the 3D calving model presented here solves the full-Stokes stress solution, making it complex to implement and computationally expensive. However, our results indicate that Store Glacier is sensitive to processes such as concentrated plume melting and laterally variable topography, which cannot be represented in flowline models, as well as buoyant bending forces (James et al., 2014) and ice cliff force imbalance (DeConto & Pollard, 2016), which cannot be directly represented in vertically integrated models. Thus, the goal of implementing calving into ice-sheet models demands a compromise between fidelity and efficiency.

The calving dynamics of Store Glacier have previously been investigated by Morlighem et al. (2016), using a 2D plan-view model (ISSM). Comparing results from ISSM and the present study may help guide future calving model development. The calving law used by Morlighem et al. (2016) combines a velocity and stress dependent calving rate, and a hydrostatic condition which enforces calving when flotation is reached. Despite the difference in calving law and model physics, there are some similarities in model behaviour. In both models, terminus position displays a seasonal cycle in response to variations in submarine melt rate, and the glacier terminus is interannually stable under present-day forcing. In both models, the stable terminus position is close to observed, although in the ISSM case this is because the model forces calving when flotation occurs. This may also explain the mismatch between ISSM and observed terminus position in the southern half, which our model predicts to be floating.

The 2D plan view model of Morlighem et al. (2016) is less computationally demanding than our full-Stokes approach; if the calibration of the calving law could be shown to be universally applicable, it could feasibly be extended to the entire ice sheet. However, the vertically integrated approach does not resolve vertical stress gradients, and so cannot capture the effect of buoyant bending or ice cliff force imbalance, both of which play a critical role in our model results. Therefore, the application of lower-dimensional ice-sheet models to calving may depend on suitable parameterisations of these effects, just as large scale fjord circulation models must parameterise subgrid plume dynamics (Cowton et al., 2015). Some progress has already been made in this direction. For example, the effect of the ice cliff force imbalance on the near-terminus stress regime has received a great deal of attention (Hanson and Hooke, 2000; Hanson and Hooke, 2003; O'Leary and Christoffersen, 2013). Based on the analysis of Bassis and Walker (2012), Pollard et al. (2015) implemented parameterizations for ice cliff failure and calving into a depth-integrated model of the Antarctic Ice Sheet.

A recent study by Ahlkrona et al. (2016) presented a mixed model capable of solving the SIA and the full-Stokes equations in different parts of the same model domain. This hybrid

strategy, and the flexibility of finite element meshing, raises the possibility of developing an efficient model for an entire ice sheet which is still capable of fully resolving the stress regime at high spatial resolution where necessary. Such an approach would avoid the need for parameterised stress effects entirely.

5.5 Future Work

We have presented a new 3D calving model and demonstrated its ability to reproduce the observed calving behaviour of Store Glacier. An upcoming publication will investigate, in more detail, the glacier's sensitivity to changes in these environmental processes, and begin to address the question of Store Glacier's future stability; this sensitivity analysis is presently available in the thesis associated with this work (Todd, 2017). Our results strongly implicate submarine melting and ice mélange buttressing as important drivers of calving dynamics at Store Glacier, but more work is required to determine if these conclusions hold true for other outlet glaciers, and over longer time periods.

The calving criterion we implement in the model could be improved by incorporating stress history and damage mechanics (Krug et al., 2014). At present, the presence of crevasses does not feedback into the stress regime of the ice, and the model has no 'memory' of previous crevasse fields from which to evolve. Future work should implement and investigate these effects to determine their importance for calving modelling. Implementing more sophisticated fracture mechanics to track the growth of individual crevasses may also yield interesting insights, though this may be overly complex for large scale calving models. Recent work by Benn et al. (2017) compares the 2D Elmer/Ice calving model (Todd et al., 2014) with a state-of-the-art discrete element calving model (Åström et al., 2013). A similar analysis of the 3D model presented here would help inform future research into the nature of calving and calving laws.

6 Conclusions

The 3D calving model developed in this study successfully reproduces the observed seasonal evolution of Store Glacier's calving terminus with three simple forcings and no calibration or tuning. The model features:

- a physical, untuned calving law
- 3D full-Stokes ice dynamics
- evolving non-vertical calving front
- variable mesh resolution
- realistic environmental forcing

These features allow the model to resolve important vertical and lateral stress gradients, simulate individual calving events across a range of magnitudes, and capture the glacier's response to seasonal changes in submarine melt undercutting (distributed and concentrated) and buttressing from proglacial ice mélange.

We find that ice mélange is primarily responsible for Store Glacier's seasonal advance and retreat, and that submarine melting prevents the glacier from forming a permanent floating tongue. Concentrated plume melting can have a disproportionately large and destabilizing effect by breaking stress bridges and promoting calving. The model's response to these forcings differs from north to south due to topographic effects, with the floating southern side

displaying a greater environmental sensitivity. Modelled calving events produce icebergs whose mass spans orders of magnitude, from 'spalling' events less than a tonne up to 1.19 Gt tabular bergs.

Author Contributions

JT developed the 3D calving model with substantial help from PC, TZ and PR. The simulations were designed by JT and PC. NC provided data to constrain submarine melt rates and also provided fjord bathymetry. AH was the P.I. on projects that devised and implemented the UAV and marine data collection. DB and AL supplied TSX data used to constrain basal friction through inversions. DB also advised on the numerical parameterization of calving processes. NT provided advice on the parameterization of mélange processes. JR aided by NT provided UAV data to constrain the mélange buttressing force. DS provided the plume model and fjord stratification data to compute plume melt rates. JT wrote the paper with substantial contributions from PC and co-authors. Authors are listed according to their contribution.

Acknowledgments, Samples, and Data

References

Ahlkrona, J., Lötstedt, P., Kirchner, N., & Zwinger, T. (2016). Dynamically coupling the non-linear Stokes equations with the shallow ice approximation in glaciology: Description and first applications of the ISCAL method. *Journal of Computational Physics*, *308*, 1–19. https://doi.org/10.1016/j.jcp.2015.12.025

Alley, R. B., Horgan, H. J., Joughin, I., Cuffey, K. M., Dupont, T. K., Parizek, B. R., Anandakrishnan, S., Bassis, J. (2008). A Simple Law for Ice-Shelf Calving. *Science*, *322*(5906), 1344–1344. https://doi.org/10.1126/science.1162543

Amundson, J. M., Fahnestock, M., Truffer, M., Brown, J., Lüthi, M. P., & Motyka, R. J. (2010). Ice mélange dynamics and implications for terminus stability, Jakobshavn Isbræ, Greenland. *Journal of Geophysical Research: Earth Surface*, 115(F1).

Åström, J. A., Riikilä, T. I., Tallinen, T., Zwinger, T., Benn, D., Moore, J. C., & Timonen, J. (2013). A particle based simulation model for glacier dynamics. Cryosphere. https://doi.org/10.5194/tc-7-1591-2013

Bassis, J. N., Fricker, H. A., Coleman, R., & Minster, J. B. (2008). An investigation into the forces that drive ice-shelf rift propagation on the amery ice shelf, East Antarctica. *Journal of Glaciology*, *54*(184), 17–27.

Bassis, J. N., & Walker, C. C. (2012). Upper and lower limits on the stability of calving glaciers from the yield strength envelope of ice. *Proceedings of the Royal Society A: Mathematical, Physical and Engineering Sciences*, *468*(2140), 913–931. https://doi.org/10.1098/rspa.2011.0422

Bassis, J. N., & Jacobs, S. (2013). Diverse calving patterns linked to glacier geometry. *Nature Geoscience*. https://doi.org/10.1038/ngeo1887

Benn, D. I., Hulton, N. R. J., & Mottram, R. H. (2007a). "Calving laws","sliding laws" and the stability of tidewater glaciers. *Annals of Glaciology*, 46(1), 123–130.

Benn, D. I., Warren, C. R., & Mottram, R. H. (2007b). Calving processes and the dynamics of calving glaciers. Earth-Science Reviews, 82(3–4), 143–179.

Benn, D. I., Åström, J., Zwinger, T., Todd, J., Nick, F. M., Cook, S., Hulton, N. & Luckman, A. (2017). Melt-under-cutting and buoyancy-driven calving from tidewater glaciers: new insights from discrete element and continuum model simulations. *Journal of Glaciology*, *63*(240), 691-702.

Blatter, H. (1995). Velocity and stress fields in grounded glaciers: a simple algorithm for including deviatoric stress gradients. *Journal of Glaciology*, *41*(138), 333–344. https://doi.org/10.3198/1995JoG41-138-333-344

Borstad, C. P., Khazendar, A., Larour, E., Morlighem, M., Rignot, E., Schodlok, M. P., & Seroussi, H. (2012). A damage mechanics assessment of the Larsen B ice shelf prior to collapse: Toward a physically-based calving law. *Geophysical Research Letters*, *39*(17).

Brown, C. S., Meier, M. F., Post, A., & Survey, G. (1982). *Calving speed of Alaska tidewater glaciers, with application to Columbia Glacier*. US Dept. of the Interior, Geological Survey.

Carr, J. R., Vieli, A., & Stokes, C. (2013). Influence of sea ice decline, atmospheric warming, and glacier width on marine-terminating outlet glacier behavior in northwest Greenland at seasonal to interannual timescales. *Journal of Geophysical Research: Earth Surface*, *118*(3), 1210–1226. https://doi.org/10.1002/jgrf.20088

Cook, S., Zwinger, T., Rutt, I. C., O'Neel, S., & Murray, T. (2012). Testing the effect of water in crevasses on a physically based calving model. *Annals of Glaciology*, *53*(60), 90–96. https://doi.org/10.3189/2012AoG60A107

Cook, S., Rutt, I. C., Murray, T., Luckman, A., Zwinger, T., Selmes, N., James, T. D. (2014). Modelling environmental influences on calving at Helheim Glacier in eastern Greenland. *The Cryosphere*, *8*(3), 827–841. https://doi.org/10.5194/tc-8-827-2014

Cornford, S. L., Martin, D. F., Graves, D. T., Ranken, D. F., Le Brocq, A. M., Gladstone, R. M., Payne, A. J., Ng, E. G., Lipscomb, W. H. (2013). Adaptive mesh, finite volume modeling of marine ice sheets. *Journal of Computational Physics*, *232*(1), 529–549. https://doi.org/10.1016/j.jcp.2012.08.037

Chapuis, A., & Tetzlaff, T. (2014). The variability of tidewater-glacier calving: Origin of event-size and interval distributions. *Journal of Glaciology*, *60*(222), 622–634. https://doi.org/10.3189/2014JoG13J215

Chauché, N. (2016). *Glacier-Ocean interaction at Store Glacier (West Greenland)*. PhD thesis, Aberystwyth University, http://cadair.aber.ac.uk/dspace/handle/2160/42621.

Christoffersen, P., Mugford, R. I., Heywood, K. J., Joughin, I., Dowdeswell, J. A., Syvitski, J. P. M., … Benham, T. J. (2011). Warming of waters in an East Greenland fjord prior to glacier retreat: mechanisms

and connection to large-scale atmospheric conditions. *The Cryosphere*, *5*(3), 701–714. https://doi.org/10.5194/tc-5-701-2011

Cowton, T., Slater, D., Sole, A., Goldberg, D., & Nienow, P. (2015). Modeling the impact of glacial runoff on fjord circulation and submarine melt rate using a new subgrid-scale parameterization for glacial plumes. *Journal of Geophysical Research: Oceans*, *120*(2), 796–812. https://doi.org/10.1002/2014JC010324

Cuffey, K.M. and Paterson, W.S.B., (2010). *The physics of glaciers, Fourth Edition*. Academic Press.

Deconto, R. M., & Pollard, D. (2016). Contribution of Antarctica to past and future sea-level rise. *Nature*, *531*(7596), 591–597. https://doi.org/10.1038/nature17145

Depoorter, M. A., Bamber, J. L., Griggs, J. A., Lenaerts, J. T. M., Ligtenberg, S. R. M., van den Broeke, M. R., & Moholdt, G. (2013). Calving fluxes and basal melt rates of Antarctic ice shelves. *Nature*, *502*(7469), 89–92. Retrieved from http://www.ncbi.nlm.nih.gov/pubmed/24037377

Durand, G., Gagliardini, O., Zwinger, T., Le Meur, E., & Hindmarsh, R. C. a. (2009a). Full Stokes modeling of marine ice sheets: influence of the grid size. *Annals of Glaciology*, *50*(52), 109–114. https://doi.org/10.3189/172756409789624283

Durand, G., Gagliardini, O., de Fleurian, B., Zwinger, T., & Le Meur, E. (2009b). Marine ice sheet dynamics: Hysteresis and neutral equilibrium. *Journal of Geophysical Research*, *114*(F3), F03009. https://doi.org/10.1029/2008JF001170

Enderlin, E. M., Howat, I. M., Jeong, S., Noh, M.-J., van Angelen, J. H., & van den Broeke, M. R. (2014). An Improved Mass Budget for the Greenland Ice Sheet. *Geophysical Research Letters*, *41*(3), 866–872. https://doi.org/10.1002/2013GL059010

Favier, L., Gagliardini, O., Durand, G., & Zwinger, T. (2012). A three-dimensional full Stokes model of the grounding line dynamics: effect of a pinning point beneath the ice shelf. *The Cryosphere*, *6*(1), 101–112. https://doi.org/10.5194/tc-6-101-2012

Gagliardini, O., Cohen, D., Råback, P., & Zwinger, T. (2007). Finite-element modeling of subglacial cavities and related friction law. *Journal of Geophysical Research: Earth Surface*, *112*(F2), F02027.

Gagliardini, O., Zwinger, T., Gillet-Chaulet, F., Durand, G., Favier, L., de Fleurian, B., Greve, R., Malinen, M., Martín, C., Råback, P., Ruokolainen, J., Sacchettini, M., Schäfer, M., Seddik, H., Thies, J. (2013). Capabilities and performance of Elmer/Ice, a new-generation ice sheet model. *Geoscientific Model Development*, *6*(4), 1299–1318. https://doi.org/10.5194/gmd-6-1299-2013

Geuzaine, C., & Remacle, J.-F. (2009). Gmsh: A 3-D finite element mesh generator with built-in pre- and post-processing facilities. *International Journal for Numerical Methods in Engineering*, *79*(11), 1309–1331. https://doi.org/10.1002/nme.2579

Gillet-Chaulet, F., Gagliardini, O., Seddik, H., Nodet, M., Durand, G., Ritz, C., Zwinger, T., Greve, R., Vaughan, D. G. (2012). Greenland ice sheet contribution to sea-level rise from a new-generation ice-sheet model. *The Cryosphere*, *6*(6), 1561–1576. https://doi.org/10.5194/tc-6-1561-2012

Gudmundsson, G. H., Krug, J., Durand, G., Favier, L., & Gagliardini, O. (2012). The stability of grounding lines on retrograde slopes. *Cryosphere*, *6*(6), 1497–1505.

Greve, R. (2005). Relation of measured basal temperatures and the spatial distribution of the geothermal heat flux for the Greenland ice sheet. *Annals of Glaciology*, *42*(1), 424–432. https://doi.org/10.3189/172756405781812510

Hanson, B., & Hooke, R. L. (2000). Glacier calving: A numerical model of forces in the calving-speed/water-depth relation. *Journal of Glaciology*, *46*(153), 188–196.

Hanson, B., & Hooke, R. L. (2003). Buckling rate and overhang development at a calving face. *Journal of Glaciology*, *49*(167), 577–586. https://doi.org/10.3189/172756503781830476

Holland, D. M., Thomas, R. H., de Young, B., Ribergaard, M. H., & Lyberth, B. (2008). Acceleration of Jakobshavn Isbræ triggered by warm subsurface ocean waters. *Nature Geoscience*, *1*(10), 659–664. https://doi.org/https://doi.org/10.1038/ngeo316

Howat, I. M., Box, J. E., Ahn, Y., Herrington, A., & McFadden, E. M. (2010). Seasonal variability in the dynamics of marine-terminating outlet glaciers in Greenland. *Journal of Glaciology*, *56*(198), 601–613.

Howat, I., A. Negrete, and B. Smith. 2015. *MEaSURES Greenland Ice Mapping Project (GIMP) Digital Elevation Model, Version 1*. Boulder, Colorado USA. NASA National Snow and Ice Data Center Distributed Active Archive Center. doi: http://dx.doi.org/10.5067/NV34YUIXLP9W

Hubbard, A., Ryan, J., Toberg, N., Todd, J., Christoffersen, P., Snooke, N. & Box, J. E. 2015. Tidewater Dynamics at Store Glacier, West Greenland from Daily Repeat UAV Survey. *AGU Fall Meeting Abstracts* 2015AGUFM.C33G..03H.

IPCC. (2013). *Climate Change 2013: The Physical Science Basis. Contribution of Working Group I to the IPCC Fifth Assessment Report of the Intergovernmental Panel on Climate Change, edited by: Stocker, T.F., Qin, D., Plattner, G.-K., Tignor, M., Allen, S.K., Boschung, J*. (T. F. Stocker, D. Qin, G.-K. Plattner, M. Tignor, S. K. Allen, J. Boschung, P. M. Midgley, Eds.) (Vol. AR5). Cambridge University Press, Cambridge, United Kingdom and New York, NY, USA.

James, T. D., Murray, T., Selmes, N., Scharrer, K., & O'Leary, M. (2014). Buoyant flexure and basal crevassing in dynamic mass loss at Helheim Glacier. *Nature Geoscience*, *7*(8), 593–596.

Jenkins, A. (2011). Convection-Driven Melting near the Grounding Lines of Ice Shelves and Tidewater Glaciers. *Journal of Physical Oceanography*, *41*(12), 2279–2294. https://doi.org/10.1175/JPO-D-11-03.1

Levermann, A., Albrecht, T., Winkelmann, R., Martin, M. A., Haseloff, M., & Joughin, I. (2012). Kinematic first-order calving law implies potential for abrupt ice-shelf retreat. *The Cryosphere*, *6*(2), 273–286. https://doi.org/10.5194/tc-6-273-2012

Löhner, R. (1995). Robust, Vectorized Search Algorithms for Interpolation on Unstructured Grids. *Journal of Computational Physics*, 118(2), 380–387. https://doi.org/10.1006/jcph.1995.1107

Luckman, A., Benn, D. I., Cottier, F., Bevan, S., Nilsen, F., & Inall, M. (2015). Calving rates at tidewater glaciers vary strongly with ocean temperature. *Nature Communications*, 6, 8566. https://doi.org/10.1038/ncomms9566

Krug, J., Weiss, J., Gagliardini, O., & Durand, G. (2014). Combining damage and fracture mechanics to model calving. *The Cryosphere*, *8*, 2101–2117. https://doi.org/10.5194/tcd-8-1631-2014

Krug, J., Durand, G., Gagliardini, O., & Weiss, J. (2015). Modelling the impact of submarine frontal melting and ice mélange on glacier dynamics. *Cryosphere*, *9*(3), 989–1003. https://doi.org/10.5194/tc-9-989-2015

Ma, Y., Tripathy, C. S., & Bassis, J. N. (2017). Bounds on the calving cliff height of marine terminating glaciers. Geophysical Research Letters, 44(3), 1369–1375. https://doi.org/10.1002/2016GL071560

McFadden, E. M., Howat, I. M., Joughin, I., Smith, B. E., & Ahn, Y. (2011). Changes in the dynamics of marine terminating outlet glaciers in west Greenland (2000–2009). *Journal of Geophysical Research*, *116*(F2), F02022. https://doi.org/10.1029/2010JF001757

Moon, T., Joughin, I., & Smith, B. (2015). Seasonal to multiyear variability of glacier surface velocity, terminus position, and sea ice/ice mélange in northwest Greenland. *Journal of Geophysical Research: Earth Surface*, *120*(5), 818–833. https://doi.org/10.1002/2015JF003494

Morlighem, M., Bondzio, J., Seroussi, H., Rignot, E., Larour, E., Humbert, A., & Rebuffi, S. (2016). Modeling of Store Gletscher's calving dynamics, West Greenland, in response to ocean thermal forcing. *Geophysical Research Letters*, *43*(6), 2659–2666.

Mottram, R. H., & Benn, D. I. (2009). Testing crevasse-depth models: a field study at Breiðamerkurjökull, Iceland. *Journal of Glaciology*, *55*(192), 746–752. https://doi.org/10.3189/002214309789470905

Motyka, R. J. (1997). Deep-water calving at Le Conte Glacier, Southeast Alaska. In *Calving glaciers: report of a workshop* (pp. 115–118).

Nick, F. M., Van der Veen, C. J., Vieli, A., & Benn, D. I. (2010). A physically based calving model applied to marine outlet glaciers and implications for the glacier dynamics. *Journal of Glaciology*, *56*(199), 781–794.

Noël, B., van de Berg, W. J., van Meijgaard, E., Kuipers Munneke, P., van de Wal, R. S. W., & van den Broeke, M. R. (2015). Evaluation of the updated regional climate model RACMO2.3: summer snowfall impact on the Greenland Ice Sheet. *The Cryosphere*, *9*(5), 1831–1844. https://doi.org/10.5194/tc-9-1831-2015

Nye, J. F. (1957). The Distribution of Stress and Velocity in Glaciers and Ice-Sheets. *Proceedings of the Royal Society A: Mathematical, Physical and Engineering Sciences*, *239*(1216), 113–133. https://doi.org/10.1098/rspa.1957.0026

O'Leary, M., & Christoffersen, P. (2013). Calving on tidewater glaciers amplified by submarine frontal melting. *The Cryosphere*, *7*(1), 119–128. https://doi.org/10.5194/tc-7-119-2013

O'Neel, S., Echelmeyer, K. A., & Motyka, R. J. (2004). Short-term variations in calving of a tidewater glacier: LeConte Glacier, Alaska, U.S.A. *Journal of Glaciology*, *49*(167), 587–598. https://doi.org/10.3189/172756503781830430

Otero, J., Navarro, F. J., Martin, C., Cuadrado, M. L., & Corcuera, M. I. (2010). A three-dimensional calving model: numerical experiments on Johnsons Glacier, Livingston Island, Antarctica. *Journal of Glaciology*, *56*(196), 200–214. https://doi.org/10.3189/002214310791968539

Pattyn, F. (2003). A new three-dimensional higher-order thermomechanical ice sheet model: Basic sensitivity, ice stream development, and ice flow across subglacial lakes. *Journal of Geophysical Research*, *108*(B8), 1–15. https://doi.org/10.1029/2002JB002329

Pollard, D., DeConto, R. M., & Alley, R. B. (2015). Potential Antarctic Ice Sheet retreat driven by hydrofracturing and ice cliff failure. *Earth and Planetary Science Letters*, *412*, 112–121. https://doi.org/10.1016/j.epsl.2014.12.035

Rignot, E., & Kanagaratnam, P. (2006). Changes in the velocity structure of the Greenland Ice Sheet. *Science*, *311*(5763), 986–990. https://doi.org/10.1126/science.1121381

Rignot, E., Xu, Y., Menemenlis, D., Mouginot, J., Scheuchl, B., Li, X., Morlighem, M., Seroussi, H., van den Broeke, M. Fenty, I. Cai, C. An, L. Fleurian, B. de. (2016). Modeling of ocean-induced ice melt rates of five west Greenland glaciers over the past two decades. *Geophysical Research Letters*, *43*(12), 6374–6382. https://doi.org/10.1002/2016GL068784

Ryan, J. C., Hubbard, A. L., Box, J. E., Todd, J., Christoffersen, P., Carr, J. R., Holt, T. O., Snooke, N. (2015). UAV photogrammetry and structure from motion to assess calving dynamics at Store Glacier, a large outlet draining the Greenland ice sheet. *The Cryosphere*, *9*(1), 1–11. https://doi.org/10.5194/tc-9-1-2015

Seddik, H., Greve, R., Zwinger, T., Gillet-Chaulet, F., & Gagliardini, O. (2012). Simulations of the Greenland ice sheet 100 years into the future with the full Stokes model Elmer/Ice. *Journal of Glaciology*, *58*(209), 427–440. https://doi.org/10.3189/2012JoG11J177

Slater, D. A., Goldberg, D. N., Nienow, P. W., & Cowton, T. R. (2016). Scalings for Submarine Melting at Tidewater Glaciers from Buoyant Plume Theory. *Journal of Physical Oceanography*, *46*(6), 1839–1855. https://doi.org/10.1175/JPO-D-15-0132.1

Slater, D. A., Nienow, P. W., Goldberg, D. N., Cowton, T. R., & Sole, A. J. (2017). A model for tidewater glacier undercutting by submarine melting. *Geophysical Research Letters*, *44*(5), 2360–2368. https://doi.org/10.1002/2016GL072374

Toberg, Nick, et al. "Estimating ice-melange properties with repeat UAV surveys over Store Glacier, West Greenland." *EGU General Assembly Conference Abstracts.* Vol. 18. 2016.

Todd, J., & Christoffersen, P. (2014). Are seasonal calving dynamics forced by buttressing from ice mélange or undercutting by melting? Outcomes from full-Stokes simulations of Store Glacier, West Greenland. *The Cryosphere*, *8*(6), 2353–2365. https://doi.org/10.5194/tc-8-2353-2014

Todd, J. (2017). A 3D full Stokes calving model for Store Glacier, West Greenland. PhD thesis. University of Cambridge.

Turner, J. S. (1973). *Buoyancy effects in fluids. Cambridge University Press., London* (Vol. 0). Cambridge University Press., London.

Ultee, L., & Bassis, J. (2016). The future is Nye: An extension of the perfect plastic approximation to tidewater glaciers. *Journal of Glaciology*, *62*(236), 1143–1152. https://doi.org/10.1017/jog.2016.108

Van der Veen, C. J. (1996). Tidewater calving. *Journal of Glaciology*, *42*(141), 375–385.

Van der Veen, C. J. (1998a). Fracture mechanics approach to penetration of bottom crevasses on glaciers. *Cold Regions Science and Technology*, 27(3), 213–223.

Van der Veen, C. J. (1998b). Fracture mechanics approach to penetration of surface crevasses on glaciers. *Cold Regions Science and Technology*, 27(1), 31–47.

Vieli, A., Funk, M., & Blatter, H. (2001). Flow dynamics of tidewater glaciers: A numerical modelling approach. *Journal of Glaciology*, *47*(159), 595–606.

Vieli, A., & Nick, F. (2011). Understanding and modelling rapid dynamic changes of tidewater outlet glaciers: issues and implications. *Surveys in Geophysics*, *32*(4–5), 437–458.

Walter, J. I., Jason, E., Tulaczyk, S., Brodsky, E. E., Howat, I. M., Yushin, A. H. N., & Brown, A. (2012). Oceanic mechanical forcing of a marine-terminating Greenland glacier. *Annals of Glaciology*, *53*(60), 181–192.

Warren, C. R., Glasser, N. F., Harrison, S., Winchester, V., Kerr, A. R., & Rivera, A. (1995). Characteristics of Tide-Water Calving at Glaciar San-Rafael, Chile. *Journal of Glaciology*, *41*(138), 273–289.

Weidick, A., & Bennike, O. (2007). Quaternary glaciation history and glaciology of Jakobshavn Isbræ and the Disko Bugt region, West Greenland: a review. *Geological Survey of Denmark and Greenland*, *14*. Retrieved from http://www.geus.dk/publications/bull/nr14/nr14_p01-13_A1b.pdf

Zwinger, T., Greve, R., Gagliardini, O., Shiraiwa, T., & Lyly, M. (2007). A full Stokes-flow thermo-mechanical model for firn and ice applied to the Gorshkov crater glacier, Kamchatka. *Annals of Glaciology*, *45*(1), 29–37. https://doi.org/10.3189/172756407782282543

Zwinger, T., & Moore, J. C. (2009). Diagnostic and prognostic simulations with a full Stokes model accounting for superimposed ice of Midtre Lovénbreen, Svalbard. *The Cryosphere*, *3*(2), 217–229. https://doi.org/10.5194/tc-3-217-2009

Run Code	Mélange Thickness (m)	Conc. Melt Max (m d^{-1})	Dist. Melt Summer Ave (m d^{-1})	Dist. Melt Winter Ave (m d^{-1})
000	0	0	0	0
001	0	0	3.1	1.3
011	0	12	3.1	1.3
111	140	12	3.1	1.3

Table 1: Environmental forcings in each simulation. The ice mélange season spans 1st Feb - 29th May. The summer melt season spans 1st June - 31st Aug.

Run Code	Influx	Submarine Melt			Surface Melt	Toe Calving	Calving
		Distributed	Concentrated	Basal			
000	9.14	0	0	0	2.51e-2	0	8.6
001	9.18	1.74	0	0.29	2.34e-2	0.11	7.17
011	9.15	1.7	0.1	0.29	2.32e-2	0.13	6.99
111	8.96	1.77	0.11	0.3	2.39e-2	0.14	6.5

Table 2: Annual mean mass gain and loss (Gt a⁻¹) for the 4 forcing scenarios, for the region beyond the flux gate shown in Figure 5. The mass loss terms do not sum exactly to the influx due to changes in terminus position from the beginning to the end of the 5 year simulations.
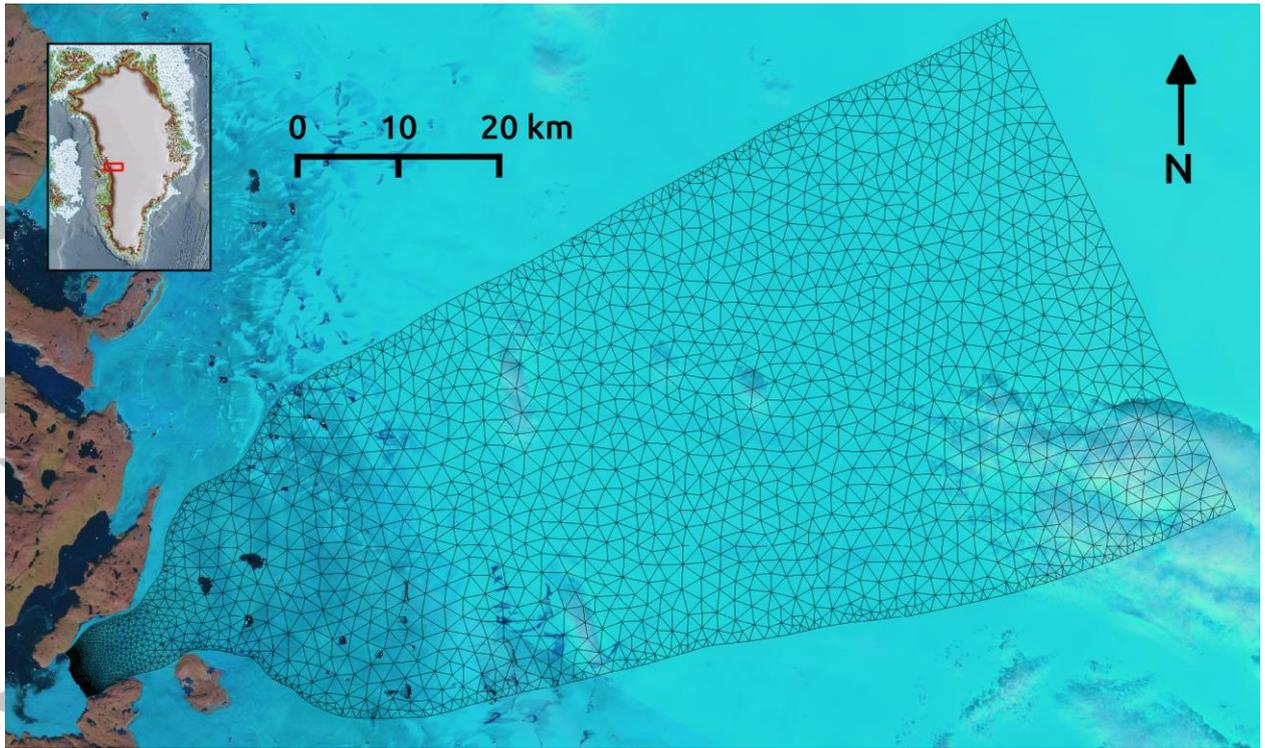
Figure 1: Plan view of the 3D model mesh of Store Glacier. The mesh resolution increases significantly towards the terminus.
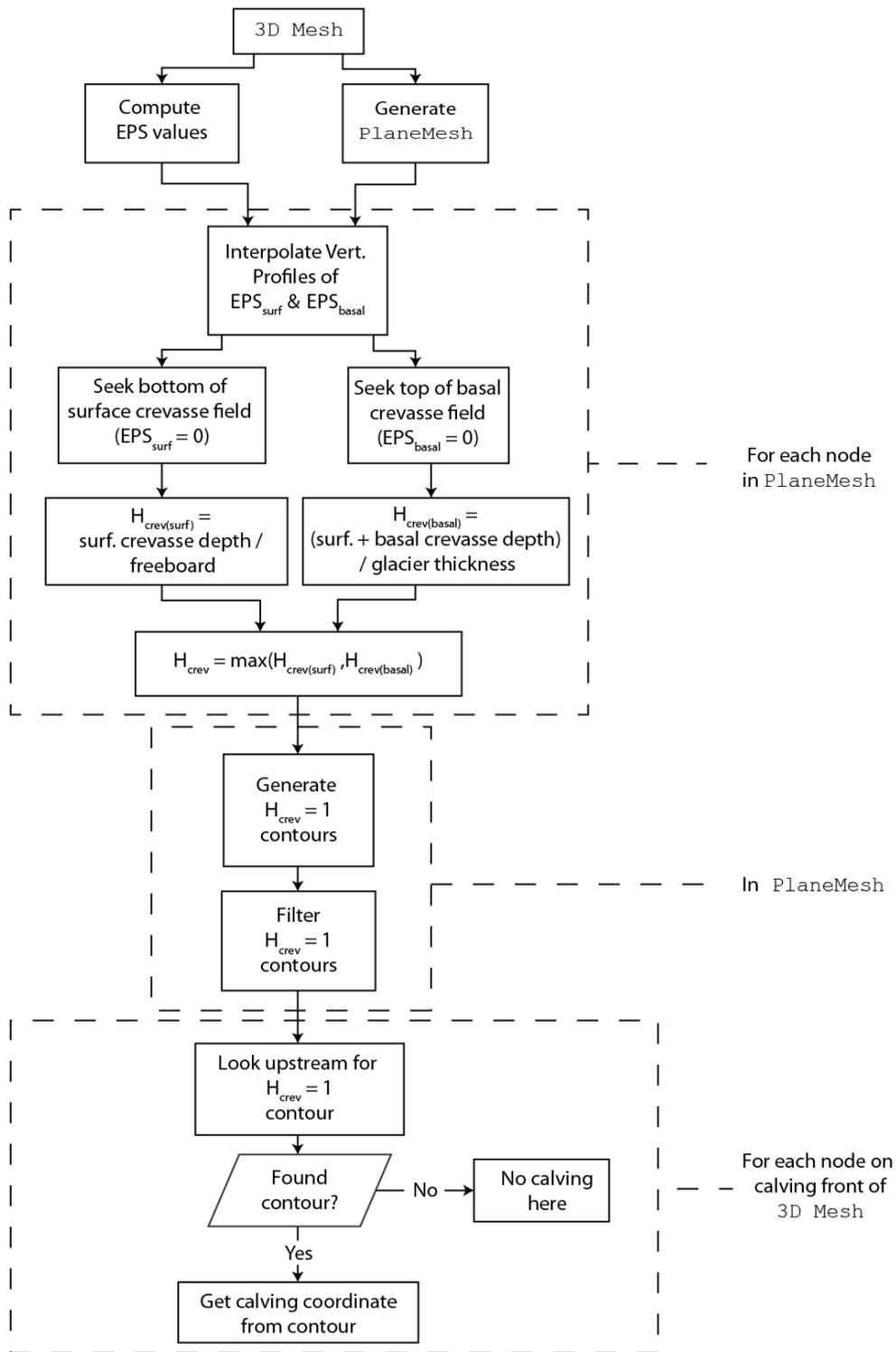
Figure 2: The full calving algorithm implemented in Calving3D
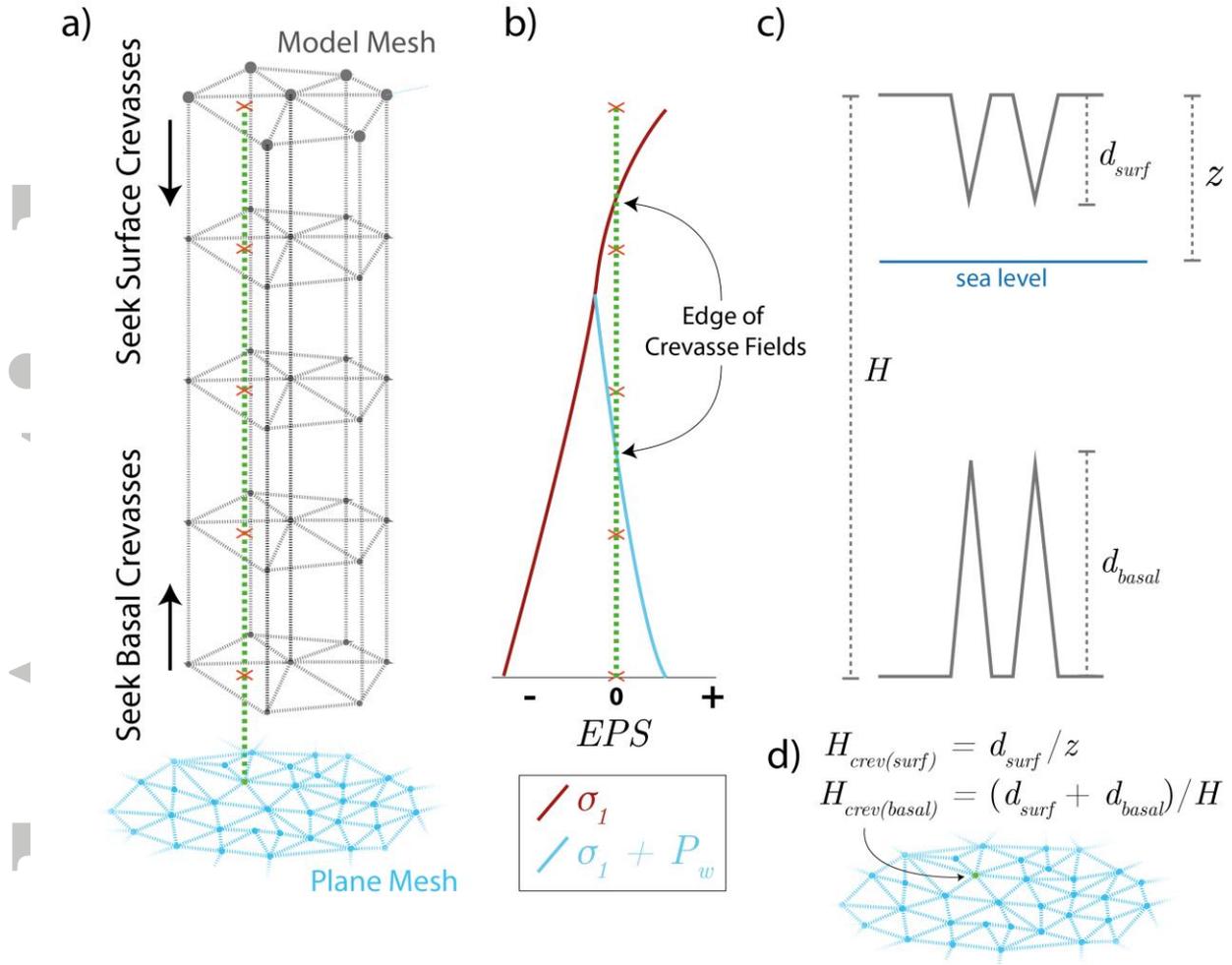
Figure 3: Schematic showing 3D calving algorithm. a) For each node in PlaneMesh, vertical intersections with 3D mesh are identified via ray casting. b) Surface/basal crevasses exist to the depth/height where net stress (EPS) is 0. c) The proportional crevasse penetration (H_{crev}) is computed from the thickness and crevasse penetration and d) this is set on the relevant node of the PlaneMesh.
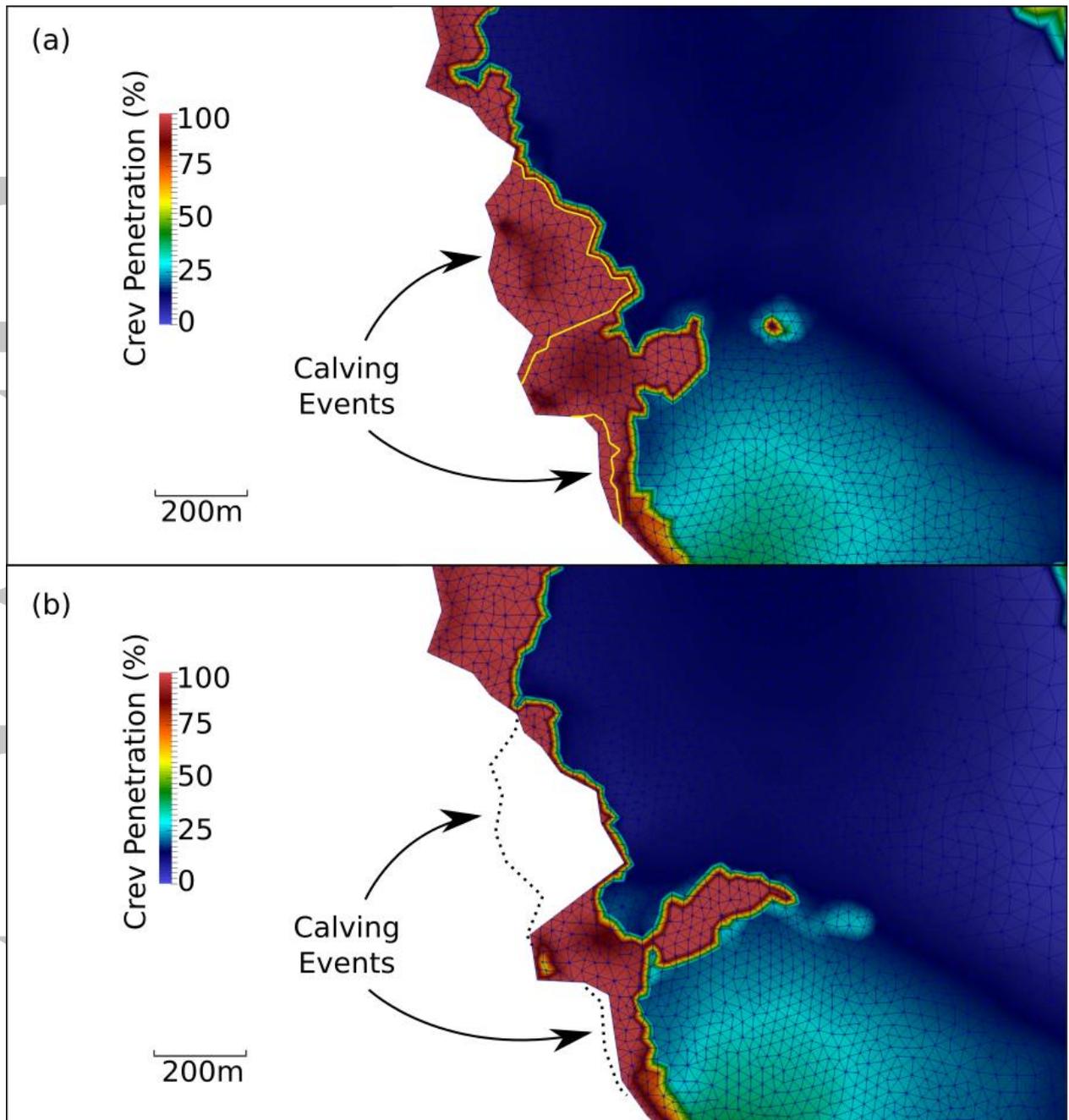
Fig. 4: Crevasse penetration (%) on PlaneMesh. a) Two concurrent calving events are delineated by yellow lines (the $H_{crev} = 1$ contour) b) Crevasse penetration in subsequent timestep. The calving events have expanded crevassing in the surrounding ice.
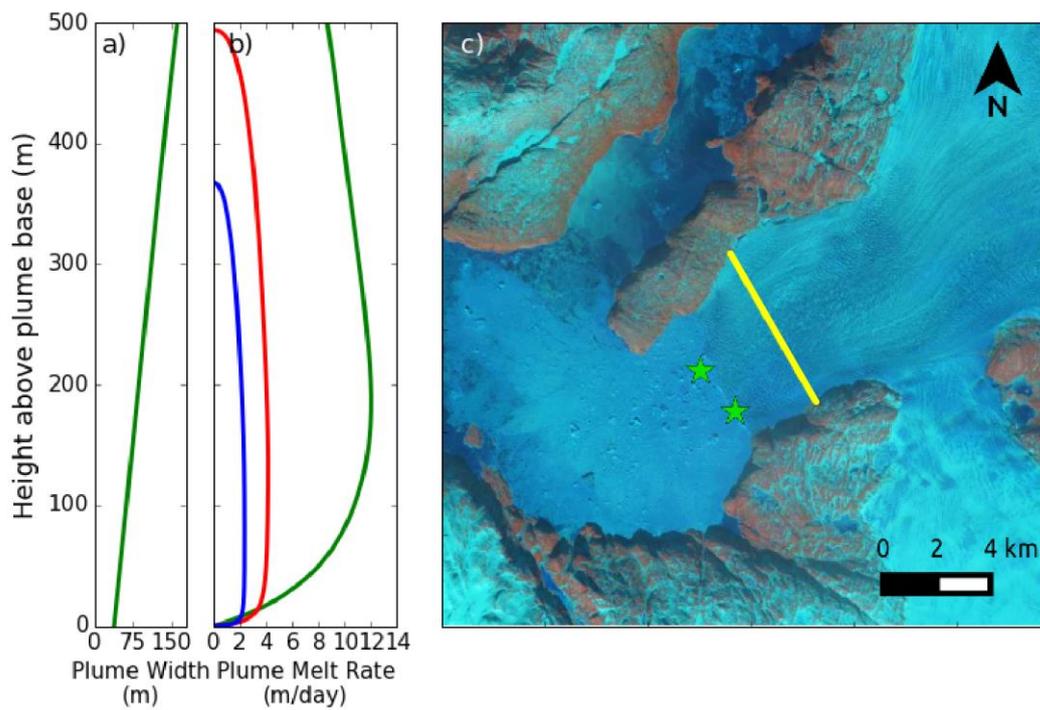
Figure 5: a) Vertical profile of conical plume width. b) Melt profiles for concentrated plumes (green), and distributed plumes in summer (red) and winter (blue). c) Green stars show location of the two persistent concentrated conical plumes observed at Store Glacier. Yellow line indicates flux gate used in analysis.
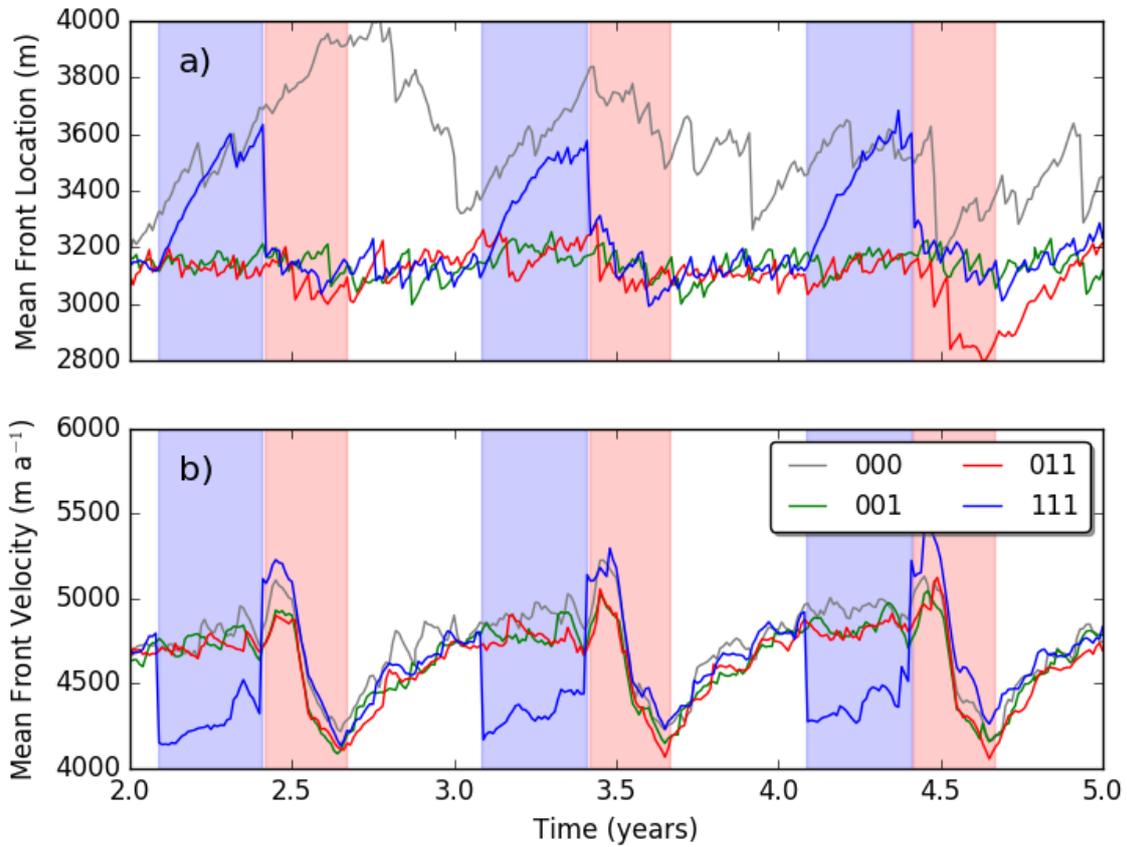
Figure 6: Mean terminus position (a) and velocity (b) for the four forcing combinations (Table 1) over the final 3 years of the simulations. Mean terminus position is relative to the flux gate shown in Fig. 5. Blue and red shading delineate the ice mélange and summer melt season, respectively. Run 000: No Forcing; Run 001: Distributed Melt Only; Run 011: Distributed and Concentrated Melt; Run 111: Distributed and Concentrated Melt as well as Mélange
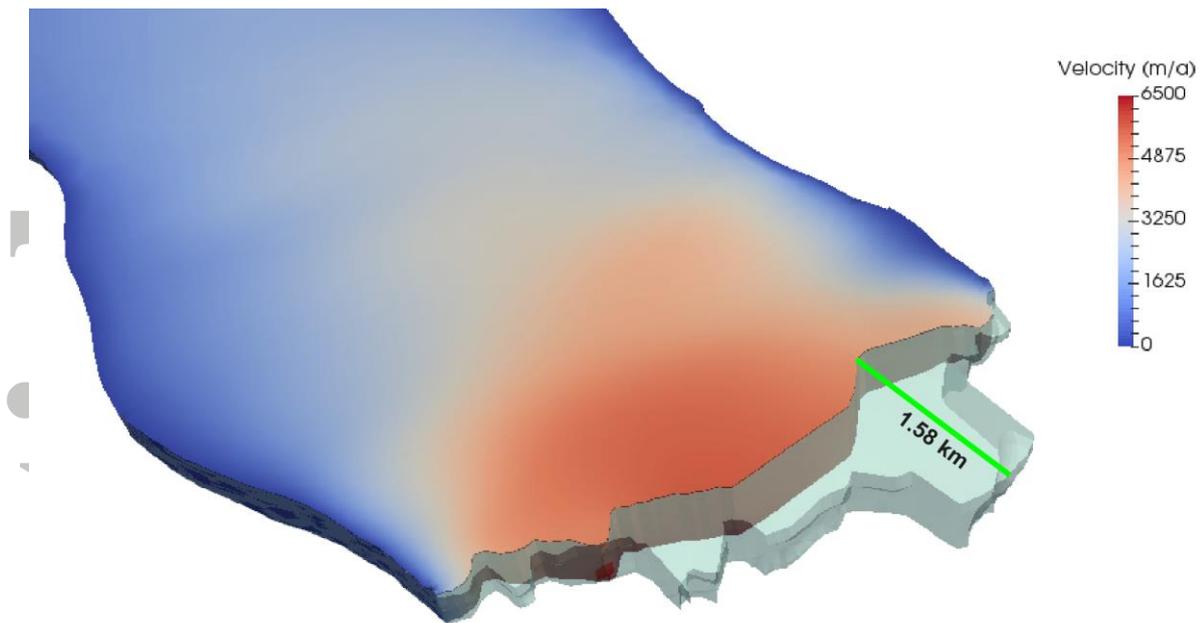
Figure 7: Rendering of model terminus showing large tabular calving event at 1.41 years of simulation 111. Transparent region defines the geometry of the tabular berg (and additional concurrent bergs) released following the ice mélange collapse. The large tabular berg is 1.6 km long in the flow direction, with a mass of 1.14 Gt and a volume of 1.28×10^9 m^3.
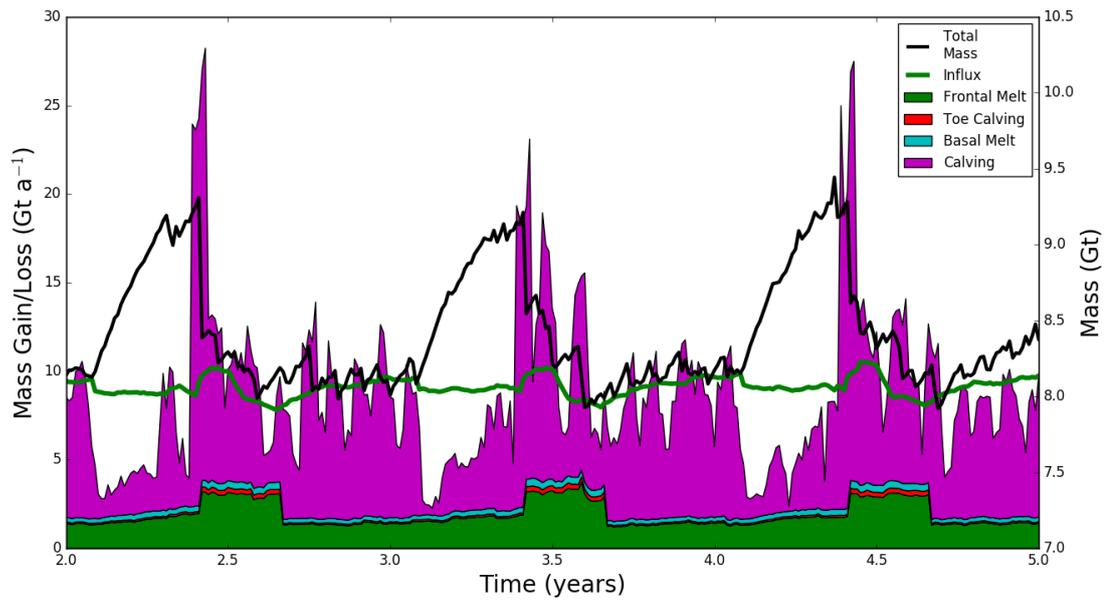
Figure 8: Components of mass loss near the terminus (shaded regions), influx through the flux gate shown in Fig. 5 (green line), and glacier mass beyond the gate (black line) for present-day forcing scenario (Run 111). Changes in total mass beyond the flux gate correspond to advance and retreat of the terminus, but the absolute value is irrelevant, given the arbitrary choice of flux gate. The negligible contribution from surface melting beyond the flux gate is omitted. For the sake of visual clarity, calving mass loss is smoothed by a moving average with a window size of 5 timesteps (0.05 year window), as calving losses from tabular bergs up to 1.58 km in length and mass up to 1.14 Gt can dwarf all other ablation processes in a given timestep.
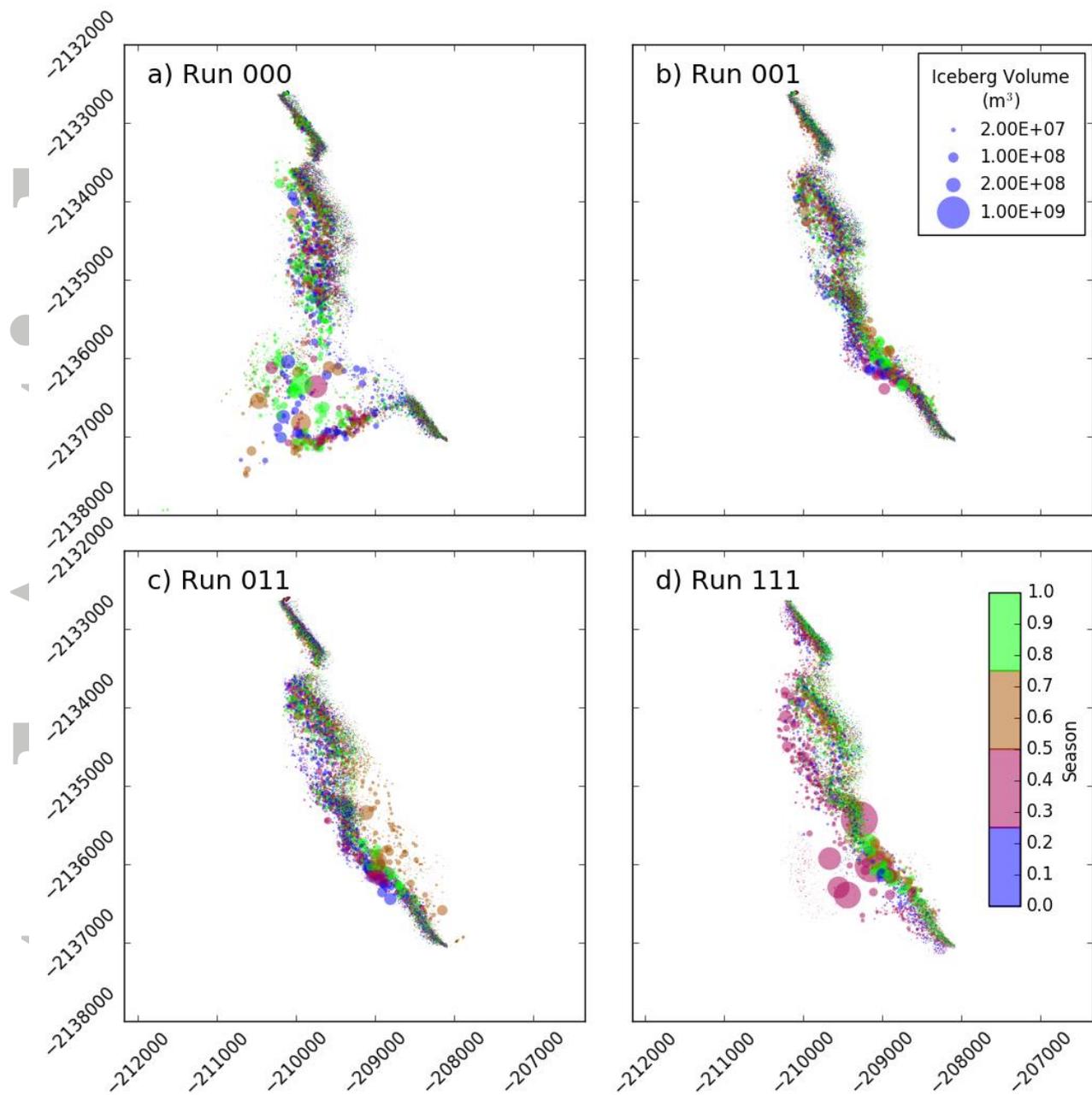
Figure 9: Calving event locations and season for all 5 years for the 4 forcing combinations: a) Run 000 b) Run 001 c) Run 011 d) Run 111.
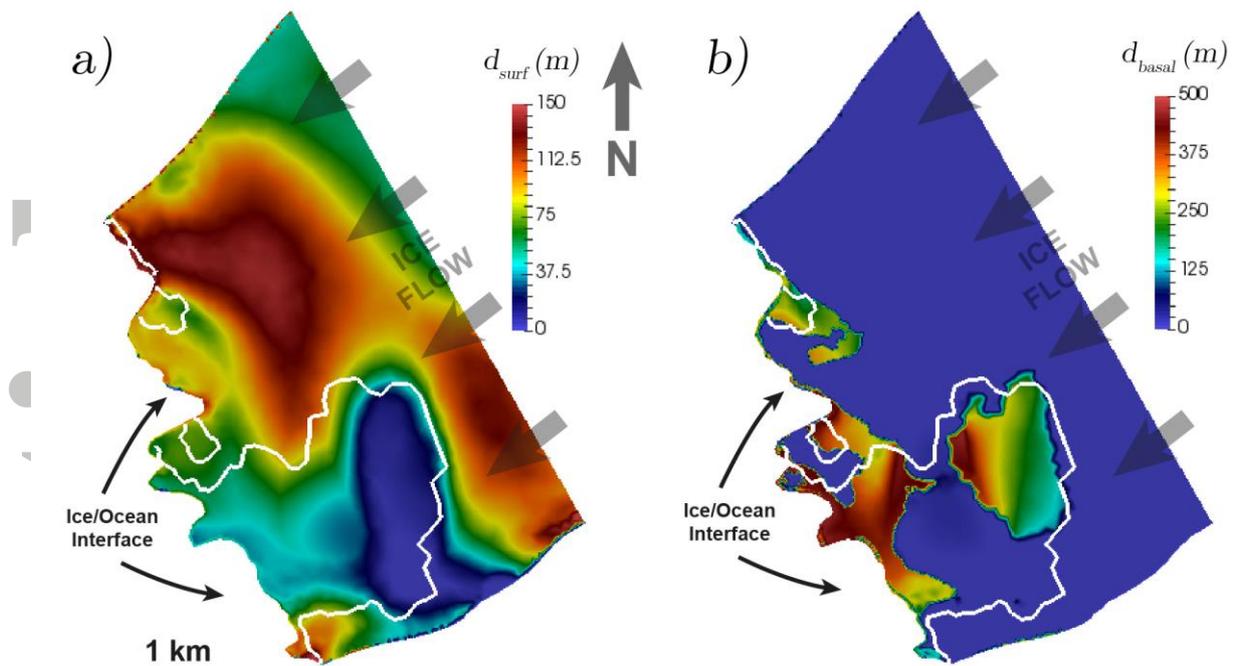
Figure 10: Depth of surface crevasses (a) and height of basal crevasses (b) from the present day experiment (Run 111, t=0.09 years). White line indicates grounding line. The two types of crevasses show distinctly different patterns. Surface crevasses are widespread and tend to vary smoothly in depth. Deepest surface crevasses occur where ice flows over bedrock rises. Basal crevasses are much more localised and there are sharp transitions between intact basal ice and deep basal crevassing. Calving in the model occurs when surface crevasses reach the water line or when surface and basal crevasses intersect. Note different colour scales.
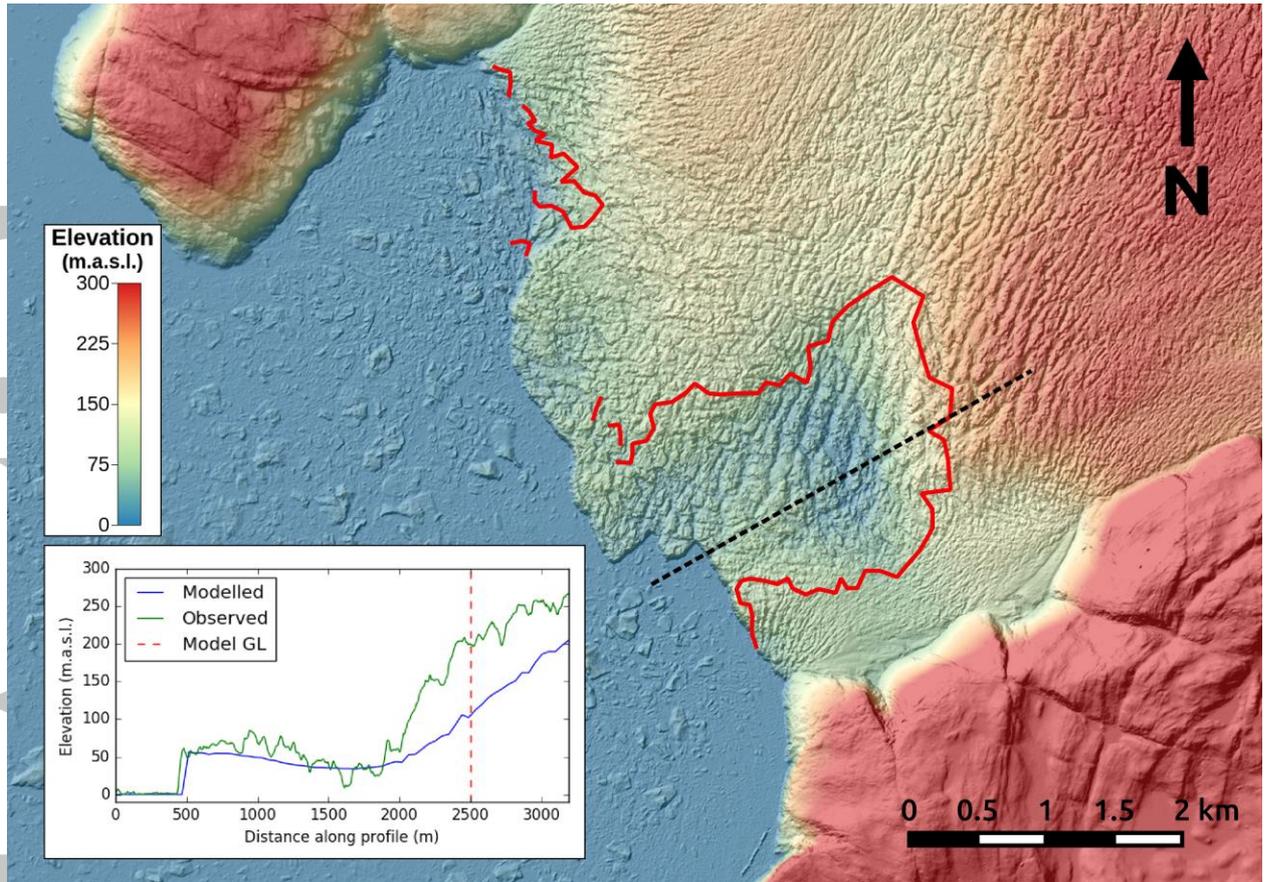
Fig 11: Observed surface DEM showing extensive surface crevassing and prominent surface depression in south, overlain with modelled grounding line (red line) (Run 111, 1.58 years). **Inset:** Elevation profile compares modelled (blue) and observed (green) surface elevation along black-dashed profile, with modelled grounding line (dashed red). Surface elevation reaches a minimum upstream of the terminus, indicating a grounding line hinge point. DEM created by the Polar Geospatial Center from DigitalGlobe, Inc. imagery.
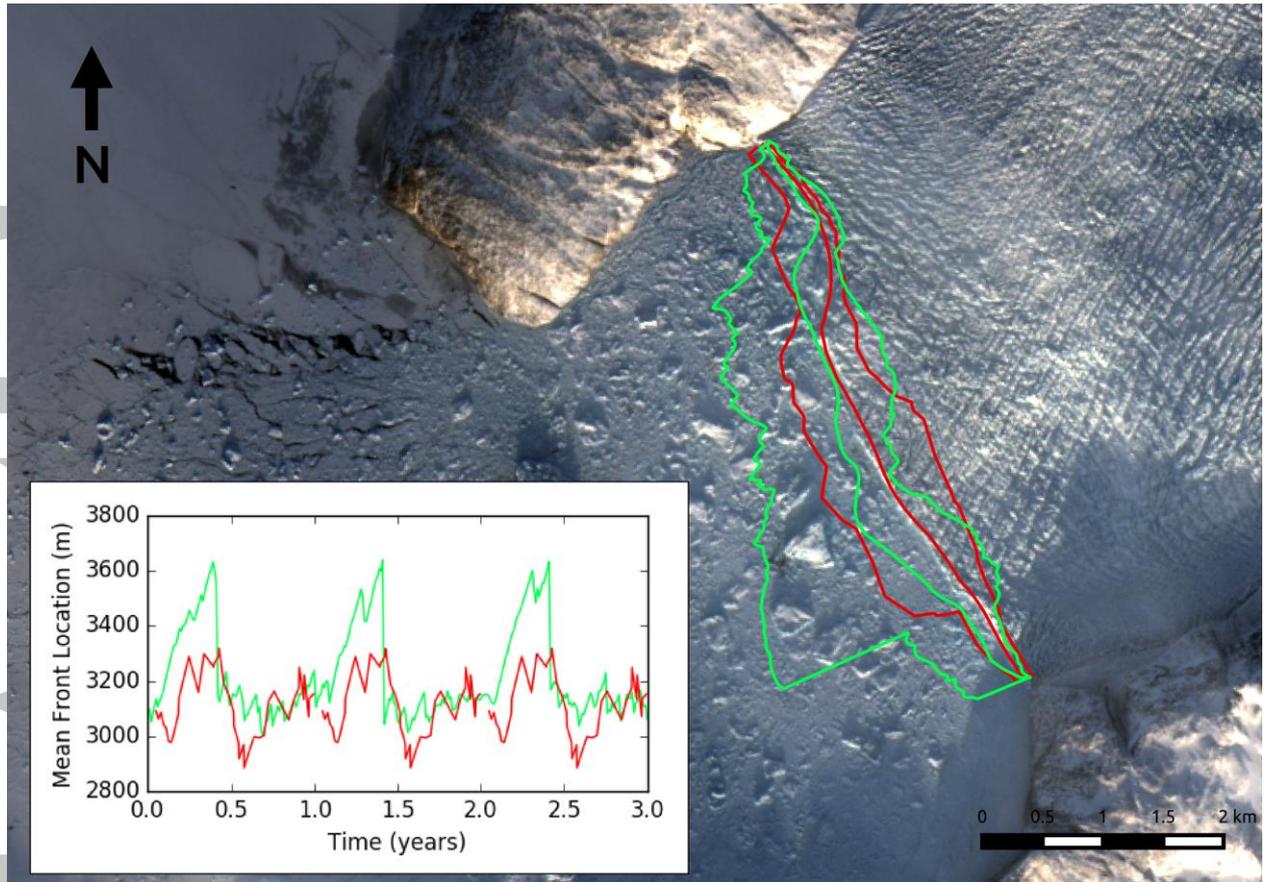
Fig 12: Modelled (green) and observed (red) maximum, mean and minimum terminus position. Observations are from 24 TSX images from April 2014 to April 2015. **Inset:** Modelled (green) and observed (red) mean terminus position through time, with respect to flux gate shown in Fig. 5. Mean model positions are from the 'present-day' simulation (Run 111), and observed positions from 2014 are repeated annually to allow for visual comparison. Imagery from Landsat 8 (USGS).